QUARKS IN HIGH ENERGY INTERACTIONS*

P.V. Landshoff
Department of Applied Mathematics and
Theoretical Physics, University of Cambridge.

Contents

1. Scope of the Lectures

The great interest of the quark parton model is that it seems to provide a successful way of relating together a variety of apparently very different reactions. In these lectures I review the principal applications of the model, which means that I discuss the following reactions:

Deep inelastic scattering of electrons, muons and neutrinos
Production of lepton pairs, J/ψ and W in hadronic collisions
Electron-positron annihilation
Large transverse momentum hadronic processes.

A striking feature of most reactions is supposed to be the presence of jets of hadrons in the final state. This jet physics is now an important area of experimental and theoretical activity, and a large part of these lectures is devoted to it. Another important area of study nowadays is the modifications to the simple parton model expected from the effects of quantum chromodynamics (QCD). I shall discuss the simple parton model first, since to a very good approxmation it seems to be sufficient to describe much of the existing data, and then consider some of the expected modifications towards the end of the lectures.

Various of the topics that I discuss are treated in much more depth in other lectures at the 1978 CERN school. I mention particularly the lectures on QCD by De Rujula and the neutrino lectures of Kleinknecht. Otherwise, more details on deep inelastic scattering may be found in my review article[1] written with Osborn, and for more about large transverse momentum there is a recent article[2] written with Jacob.

* Lectures given at the 1978 CERN school of Physics.

2. Deep Inelastic e and μ Scattering

I shall assume some familiarity with deep inelastic scattering, and I therefore give only a reminder about this subject.

Consider, then, the process

$$ep \to eX,$$

which occurs predominantly through the exchange of a single virtual photon: see figure 2.1. We are

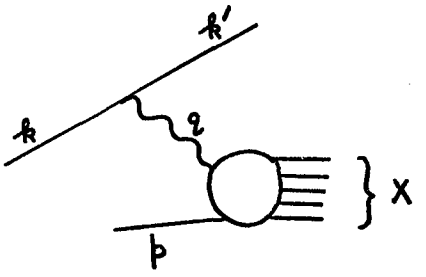

Figure 2.1. Electron or muon scattering through the exchange of a virtual photon, which is absorbed by the target hadron and causes it to break up.

interested in those events where the momentum transfer q^2 carried by the photon is large. Then the wavelength of the photon is small and so the interaction probes the short-distance structure of the nucleon target. Although it is important to explore spin effects[1], I shall confine the discussion to the case where both initial particles are unpolarised.

From the usual Feynman rules, the matrix element corresponding to figure 2.1 is

$$\mathcal{M} = [\bar{u}(k')\gamma_\alpha u(k)]\frac{g^{\alpha\mu}}{q^2} A_\mu(qp \to X), \qquad (2.1)$$

where A is the amplitude corresponding to the bubble in the figure and describes the interaction of the photon with the target. We are interested in the squared modulus of the matrix element, summed over the possible systems X of final-state hadrons. This has the form

$$\sum_X |\mathcal{M}|^2 = L_{\mu\nu}\frac{1}{q^4}W^{\mu\nu}. \qquad (2.2)$$

Here, the first factor is the leptonic part, calculated from the terms in square brackets in (2.1), and the second factor comes from the photon propagator.

These are known factors, so that the experimental data give information about $W^{\mu\nu}$, which corresponds to the interaction of the photon with the target nucleon. The term $W^{\mu\nu}$ is a sum over the hadronic systems X of the squared modulus of the amplitude A. This is depicted diagrammatically in figure 2.2, which shows also how the optical theorem relates $W^{\mu\nu}$ to the imaginary part of the forward virtual Compton-scattering amplitude.

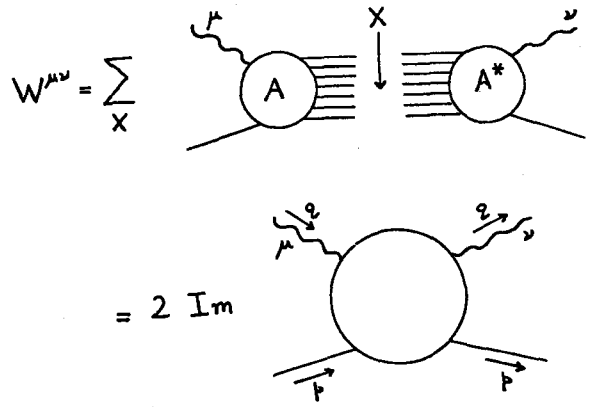

Figure 2.2. Definition of $W^{\mu\nu}$ in terms of the amplitude A of (2.1), together with its relation to the forward virtual Compton amplitude through the optical theorem.

$W^{\mu\nu}$ is a tensor, and it has the decomposition

$$W^{\mu\nu} = -\left(g^{\mu\nu} - \frac{q^\mu q^\nu}{q^2}\right) W_1 + \left(p^\mu - \frac{p\cdot q}{q^2} q^\mu\right)\left(p^\nu - \frac{p\cdot q}{q^2} q^\nu\right) W_2 . \quad (2.3)$$

Here W_1 and W_2 are two Lorentz scalar functions; they depend on the pair of Lorentz scalars q^2 and $\nu = p\cdot q$. To arrive at the decomposition (2.3), one needs, in addition to Lorentz invariance,

(i) parity conservation: this excludes a possible term $\epsilon^{\mu\nu\alpha\beta} q_\alpha p_\beta W_3$, which is present in the case of neutrino scattering.

(ii) current conservation: $q_\mu W^{\mu\nu} = W^{\mu\nu} q_\nu = 0$.

In (2.3), an average is implied over the two possible spin configurations of the target proton, as is appropriate for experiments in which the proton is unpolarised.

Notice that, because it is a momentum transfer, $q^2 < 0$. To get a feeling for the significance of $\nu = p\cdot q$, notice that in the rest frame of the target it is equal to Mq°, where q° is the energy carried by the virtual photon. It is usual to define

$$\omega = 2\nu / -q^2 . \quad (2.4)$$

Then, because baryon conservation requires that $(p+q)^2 \geq M^2$, where M is the nucleon mass, it must be that $\omega \geq 1$.

If we write

$$W_1 = F_1(\omega, q^2)$$
$$\nu W_2 = F_2(\omega, q^2), \quad (2.5)$$

then it is possible to check that both F_1 and F_2 are functions that are dimensionless. Experimentally, it is found that to a good approximation they become functions only of ω when ν and q^2 are large. This is Bjorken scaling. It implies that dependence on any fixed dimensional parameter (mass or length) has disappeared.

Figure 2.3 shows data for large ω; there is very little variation with q^2. Just how good Bjorken scaling is, and what is the nature of the deviations

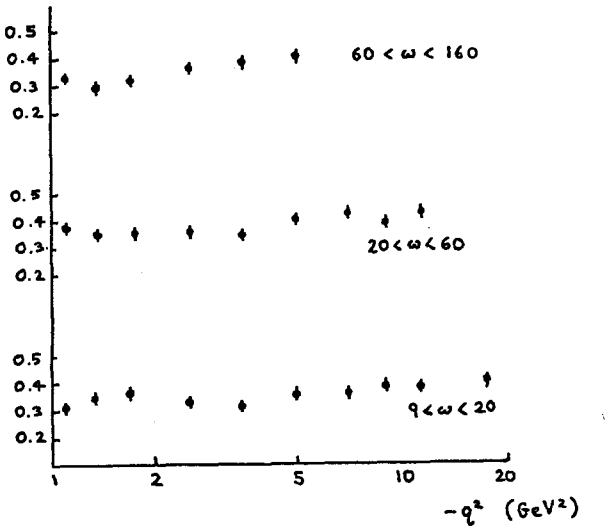

Figure 2.3. Data from $F_2(\omega, q^2)$ from the two Fermilab μp scattering experiments; see reference 3. The errors shown are statistical.

from it, is an important question in current experimental and theoretical research. Discussion of this question is obscured by the fact that Bjorken scaling is expected to be, at best, an asymptotic property, valid at rather large values of ν and q^2. Much of the data correspond to only moderate values of these variables, and this raises the question whether it is meaningful to plot such data in terms of some modified variable, say

$$\omega_a = \frac{2\nu + a}{-q^2}, \quad (2.6)$$

where a is some constant parameter. At sufficiently large ν and q^2, ω_a and ω become indistinguishable, but at small values of ω existing data seem to display Bjorken scaling much better if a is chosen

suitably than if ω is assumed to be the appropriate variable. This is shown in figure 2.4, which shows

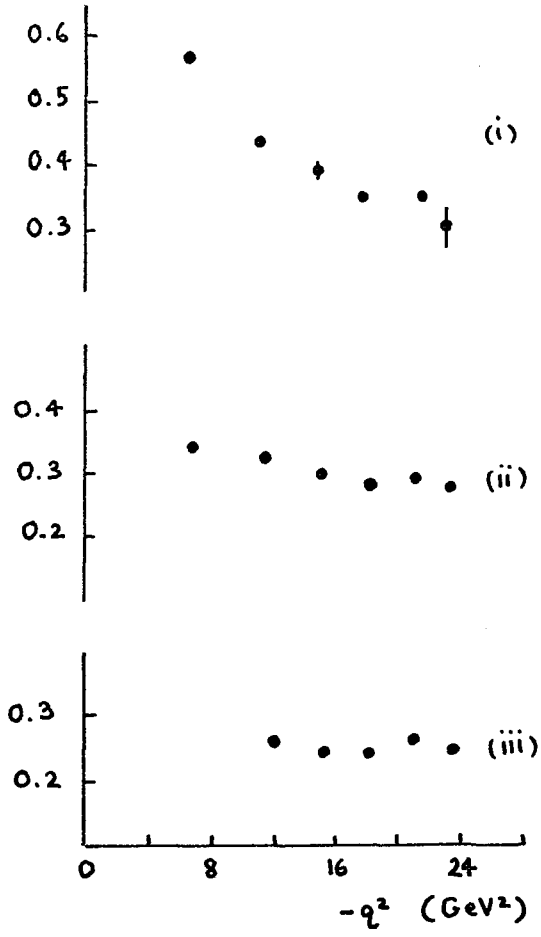

Figure 2.4. Data for $F_1(\omega, q^2)$ for ω_a^{-1} between 0.6 and 0.7, where ω_a is defined by (2.6) with the three choices (i) a = 0, (ii) a = M^2, (iii) a = 1.5 GeV^2.

the q^2 dependence of data in the range $0.6 < \omega_a^{-1} < 0.7$ for the three choices a = 0, a = M^2 and a = 1.5 GeV^2. With the last choice, there is little dependence on q^2, and the question arises whether this is significant and has a simple explanation: in terms of this variable, will the lack of dependence on q^2 survive up to very much larger values of q^2? I will return to this question in my last lecture.

3. The Parton Model

To the extent that Bjorken scaling is a valid property, so that dependence on any fixed dimensional parameter has disappeared, the conclusion is that whatever structure in the proton is responsible for scattering the photon, it has no size. This leads to the picture where the proton is composed of pointlike (or, perhaps, almost pointlike) partons. The virtual photon then scatters on one of the partons, figure 3.1.

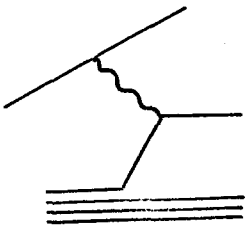

Figure 3.1. Deep Inelastic Scattering in the Parton Model.

Assume that the momentum-space wave function of the proton is sufficiently compact that, in a frame where the nucleon momentum $\underset{\sim}{p}$ is very large, the momentum of each parton is almost parallel to it. That is, before it is struck by the virtual photon the parton's momentum is approximately $x\underset{\sim}{p}$, where x is some fraction between 0 and 1. Then the energy of the parton is $(x^2\underset{\sim}{p}^2 + \mu^2)^{1/2}$, where μ is the parton mass, and for large $\underset{\sim}{p}$ this is approximately xp^0. Hence the whole parton four-momentum is almost equal to xp.

Calculating from the Feynman diagram of figure 3.1 gives

$$F_2 = Q^2 x\, \delta(x - 1/\omega), \tag{3.1}$$

where Qe is the parton charge. So scaling is obtained, and also ω^{-1} is identified as the fractional momentum x of the parton before it is struck. This last result is obtained by setting the square $(xp+q)^2$ of the 4-momentum of the parton after it is struck equal to the square of the mass of the parton.

The result (3.1) for F_2 applies whatever the spin of the parton, but the corresponding result for F_1 varies according to the spin:

$$F_1 = 0 \quad \text{spin 0 partons}$$
$$F_1 = \tfrac{1}{2}\omega F_2 \quad \text{spin } \tfrac{1}{2} \text{ partons} \tag{3.2}$$

The data[3] are in good, though not exact, agreement with the second relation. The prediction (3.2) is again an asymptotic one, valid for very large ν and q^2; the existing data satisfy it well enough to lead us to assume that spin 1/2 partons are overwhelmingly important. The study of how $(F_1 - \frac{1}{2}\omega F_2)$ varies with q^2, and the question of whether it goes to zero at very large q^2, is important but experimentally difficult; existing data do not agree too well with

each other.

Given that the partons have spin ½, the most natural and economical assumption is that they are fractionally-charged quarks, since these are already believed to be an important component of hadron structure, as a result of spectroscopic considerations. This introduces the immediate problem that the parton-model calculation seems to suppose that the parton that is struck by the photon is knocked out of the proton while, as far as is known, no fractionally-charged particles are actually present in the final state. The precise resolution of this confinement problem is not at all well understood, but it is generally believed to be something like this. The quark that is knocked out afterwards breaks up into a bunch of fragments, at least one of which must carry fractional charge. Likewise, among the remaining fragments of the proton there must be at least one that has fractional charge. See figure 3.2. A

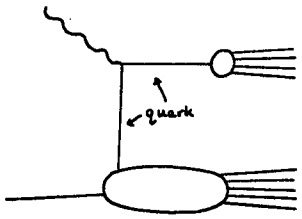

Figure 3.2. After the parton has been struck by the virtual photon, it breaks up into a system of hadrons. The quark-confining force acts between this system and the residual fragments of the target.

"confining force" acts between these two bunches of hadrons, in such a way that the fractionally-charged particles in one bunch annihilate those in the other. It is assumed, with some experimental support, that essentially only the slowest fragments in each bunch are affected by the confining force, so that for many purposes the presence of the force can be simply forgotten. I cannot emphasise too strongly that the whole question of confinement is very poorly understood, and maybe we are even wrong in believing that quarks are always confined.

The naive parton model, in which the proton is thought of as being composed of rather concrete quarks in the same way as a nucleus is composed of nucleons, is theoretically unsatisfactory. This is because the binding is rather strong, so that the situation is highly relativistic. For this reason, and in order to determine whether more fundamental theoretical ideas can confirm the model, it is useful to reformulate the model in terms of quantum field theory. After all, nowadays field theory is widely believed to provide the basis of the dynamics of particles in high energy physics.

The naive parton model calculates the cross section from the squared matrix element in the left-hand side of figure 3.3. The optical theorem says

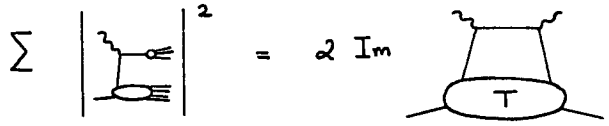

Figure 3.3. Summing the squared modulus of figure 3.2 over final states, and using the optical theorem, gives the "handbag" diagram.

that when we sum over final states we obtain the "handbag" diagram shown in the figure. In order to justify Bjorken scaling, it is necessary to establish first that the handbag diagram (with possibly some additional internal lines to represent the confining force) does indeed dominate in the large ν, large q^2 limit. Then one must also show that the handbag diagram really does scale. These questions can be examined in particular field-theory models, with the nucleon/parton-interaction amplitude T regarded as a complete sum of strong-interaction Feynman graphs.

It is found that scaling is true in ϕ^3 field theory. But this theory contains only spin-zero particles; in theories that contain spin ½ fields, necessary to describe quarks and nucleons, scaling can be badly broken. The closest that one can get to scaling is found in quantum chromodynamics[5] (QCD), where the strong interaction is mediated by the exchange of spin-one gluons, much as the electromagnetic interaction is mediated by the exchange of spin-one photons. In QCD scaling is almost satisfied. For this reason, QCD plays a central role in present-day thinking about strong interactions. But because QCD predicts that scaling is almost good, as a first approximation it is sensible to pretend that scaling really is exact, and then consider the deviations from scaling later.

Valence and Sea Quarks.

From the naive parton model,

$$F_2(x) = \sum_r Q_r^2 \left[F^{(r)}(x) + F^{(\bar{r})}(x)\right], \tag{3.3}$$

where the sum is over the various possible flavours r = u, d, s, c, ... of the struck parton and Q_r denotes the parton charge. From the calculation of figure 3.1, it is found that

$$F^{(r)}(x) = x f^{(r)}(x), \tag{3.4}$$

where $f^{(r)}(x)\,dx$ is the expectation value of the number of partons of flavour r having fractional momentum in the interval (x, x+dx). The antiquark contributions $F^{(\bar{r})}(x)$ are obtained similarly. It follows directly that

$$\int_0^1 \frac{dx}{x} F^{(r)}(x) = N^{(r)}$$

$$\int_0^1 dx\, F^{(r)}(x) = X^{(r)}, \tag{3.5}$$

where $N^{(r)}$ is the expected number of partons of flavour r in the proton and $X^{(r)}$ is the average total fractional momentum that they carry.

Experimental data show that, for the second sum rule in (3.5),

$$\sum_{r=u,d,s,c} (X^{(r)} + X^{(\bar{r})}) \simeq \tfrac{1}{2}. \tag{3.6}$$

It is widely believed that the other half of the proton's momentum is carried by the gluons. Because these are supposed to have zero charge, the virtual photon does not couple to them directly. In deep inelastic scattering, one can only hope to detect their presence indirectly, through them generating quark-antiquark pairs which themselves can couple to the photon: see figure 3.4. I shall consider this again in the last lecture, where I discuss also possible more direct ways of establishing the existence of gluons. As for the other sum rule in (3.5), Regge theory predicts that for small x, where $q^2 \ll \nu$, $F^{(r)}(x)$ and $F^{(\bar{r})}(x)$ should be dominated by pomeron exchange and so be essentially constant. The data for F_2 seem to verify this. In consequence, the first integral in (3.5) diverges at x = 0. This means that the proton contains an infinite number of quarks and antiquarks, nearly all having very small x so that they contribute little to the total momentum. That is,

$$\text{Proton} = uud + \text{"sea" of infinite number of quark-antiquark pairs}. \tag{3.7}$$

The uud are the "valence" quarks that give the proton its quantum numbers, while the sea has neutral quantum numbers. This means that

$$\begin{aligned} N^{(u)} - N^{(\bar{u})} &= 2 \\ N^{(d)} - N^{(\bar{d})} &= 1 \\ N^{(s)} - N^{(\bar{s})} &= 0 = N^{(c)} - N^{(\bar{c})}, \end{aligned} \tag{3.8}$$

and the sea contribution cancels between the two terms in each of these four relations.

Now, for a proton target

$$\begin{aligned} F_2^{ep} = {} & \left(\tfrac{2}{3}\right)^2 \left[u(x) + \bar{u}(x)\right] \\ & + \left(\tfrac{1}{3}\right)^2 \left[d(x) + \bar{d}(x) + s(x) + \bar{s}(x)\right] \\ & + c, \bar{c} \text{ terms at high energy} \end{aligned} \tag{3.9}$$

where I have written

$$u(x) = F_p^{(u)}(x) \quad \text{etc.}$$

Because the strong interactions are charge independent, charge symmetry gives

$$F_n^{(u)} = F_p^{(d)} = d(x), \quad F_n^{(d)} = F_p^{(u)} = u(x),$$
$$F_n^{(s)} = F_p^{(s)} = s(x),$$

and similarly for the antiquark contributions. Hence, for a neutron target,

$$F_2^{en} = \left(\tfrac{2}{3}\right)^2 \left[d + \bar{d}\right] + \left(\tfrac{1}{3}\right)^2 \left[u + \bar{u} + s + \bar{s}\right]. \tag{3.10}$$

Now assume (and this may be wrong) that the sea is neutral and SU(2) symmetric for each x, so that the sea contributions satisfy

$$\begin{aligned} u(x) = \bar{u}(x) = d(x) = \bar{d}(x) &= S(x) \\ s(x) = \bar{s}(x) &= S_\lambda(x). \end{aligned} \tag{3.11}$$

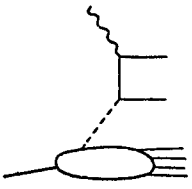

Figure 3.4. Gluons in the target hadron can generate quark-antiquark pairs, which can couple to the virtual photon.

(Maybe there is even SU(3) symmetry, so that $S = S_\lambda$, but this is hard to investigate experimentally.) Then

$$F_2^{ep} - F_2^{en} = \tfrac{1}{3}(u-d) \qquad (3.12)$$

and only valence quarks contribute to this difference. The number sum rule in (3.5) gives, from this,

$$\int_0^1 \frac{dx}{x}\left[F_2^{ep} - F_2^{en}\right] = 1/3. \qquad (3.13)$$

This seems to be satisfied experimentally, though precise neutron-target data are not available, if only because they necessarily come from deuterium targets and the Fermi-motion corrections are very large and poorly understood[6].

The literature contains many analyses of deep inelastic scattering in the valence-quark/sea-quark picture. Donnachie and I assumed[7] that the valence u and d distributions are the same shape as functions of x and so satisfy $u(x) = 2d(x) = V(x)$. Then $F_2^{ep} - F_2^{en} = \frac{1}{3}V(x)$, which may be extracted from the data, though there are large error bars. Then $F_2^{ep} = V + \frac{10}{9}S + \frac{2}{9}S_\lambda$, so that the difference between V(x) and the ep data determines the sea contribution. Our resulting curves are sketched in figure 3.5. Other authors make slightly different assumptions and interpret the data in

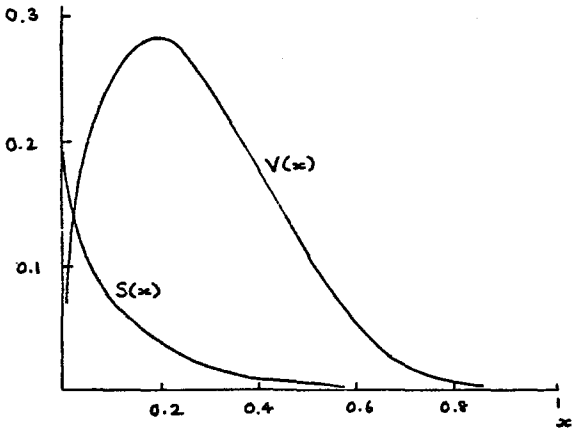

Figure 3.5. Valence and sea distributions in the nucleon, according to reference 7.

slightly different ways, and therefore obtain slightly different results. But they all agree qualitatively. The sea contributions are least well determined; the only rather sure thing is that they are very small for $x \gtrsim 2/5$.

There is room for much more work on this, by both experimentalists and theorists. Is it true that u(x) and d(x) are the same shape as functions of x, or does the ratio $d(x)/u(x)$ instead vanish as $x \to 1$? Does u(x) behave like $(1-x)^3$ as $x \to 1$, as many theorists would like[8], or is it rather $(1-x)^4$? If so, why? And how about S(x): some popular choices for the power of (1-x) here are 5, 7 or even 10. Then there are the Fermi-motion corrections for deuterium, which I have already mentioned. Lastly, there is the theoretical question of whether the decomposition "valence + sea", ignoring quantum-mechanical interference effects, can make good sense, or at least nearly so.

4. Deep Inelastic Neutrino Scattering.

Deep inelastic neutrino reactions provide a direct test of the validity of the valence-sea parton picture. There are two types of inclusive reaction, the charged-current processes

$$\nu p \to \mu^- + \text{hadrons} \quad (\text{or } e^- + \text{hadrons})$$
$$\bar{\nu} p \to \mu^+ + \text{hadrons} \quad (\text{or } e^+ + \text{hadrons}) \qquad (4.1)$$

and the neutral-current processes

$$\nu p \to \nu + \text{hadrons}$$
$$\bar{\nu} p \to \bar{\nu} + \text{hadrons} \qquad (4.2)$$

Rather more is known about the charged-current reactions than the neutral ones, both theoretically and experimentally, so I shall discuss only these. For more details, and information also on the neutral-current processes, see the lectures by Kleinknecht at this 1978 CERN School.

Just as deep inelastic e or μ scattering occurs through the exchange of a single virtual photon, neutrino scattering is believed to be mediated by the exchange of a single virtual W (figure 4.1). According to whether the incoming particle is a neutrino

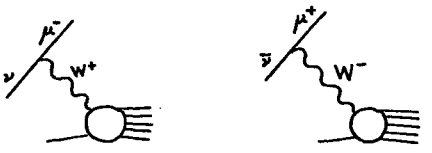

Figure 4.1. W exchange in the two reactions (4.1).

or antineutrino, the W carries charge + or -; this is why the reactions are called "charged-current". The neutral-current reactions are thought similarly to be mediated by a neutral particle, the Z_0.

The diagrams of figure 4.1 give contributions to the cross-sections that correspond to (2.2):

$$L^{\mu\nu}\,\frac{g^2}{(q^2 - M_W^2)^2}\,W_{\mu\nu}. \qquad (4.3)$$

Here, $L^{\mu\nu}$ is again the leptonic factor; it is different from the leptonic factor in (2.2) because the

W couples in a different way from the photon, but it is again known explicitly. The second factor is the W-propagator, with g the strength of its coupling. If the incident energy E is not so large that momentum transfers $-q^2$ comparable with M^2 can be achieved, a good approximation to this second factor is

$$\frac{g^2}{M_W^4} = \frac{G^2}{2}, \tag{4.4}$$

where G is the Fermi weak-interaction constant. A similar approximation is valid in the analysis of μ-decay or neutron β-decay, because there the momentum transfer is certainly small, and the value of G is, of course, well determined from these decays. A remarkable discovery of the high-energy neutrino experiments is that the structure of weak interactions deduced from the very-low-momentum-transfer decay processes gives good predictions for very much larger momentum transfers. In particular, this implies from presently available data that the W mass must be rather greater than 20 GeV.

The third factor in (4.3) describes the hadronic part of the interaction. Again, because the W and the γ have different types of coupling to hadrons, this factor is not the same as the corresponding one in (2.2). Also, it is not the same for W^+ as for W^-.

Suppose that the beam energy E is not so large that $-q^2$ can be comparable with M_W^2. If Bjorken scaling is valid, there should then be no dependence on any fixed dimensional parameter. The simplest consequence of this concerns the total cross section σ . To lowest order in the weak interactions, σ is proportional to G^2. The parameter G is not dimensionless; to obtain a cross-section it must be multiplied by a factor with the dimensions of squared momentum. Lorentz invariance demands that this factor be a Lorentz scalar, and the only available factor is therefore one proportional to $p.k$, where p and k are respectively the 4-momentum of the target proton and of the neutrino. In the laboratory frame, $p.k = ME$, so

$$\sigma \propto G^2 E. \tag{4.5}$$

Figure 4.2 shows data for σ/E for both neutrino and antineutrino beams. The result (4.5) seems to be verified.

Corresponding to (2.3), there is an expansion of $W^{\mu\nu}$:

$$W^{\mu\nu} = -g^{\mu\nu} W_1 + p^\mu p^\nu W_2 + \tfrac{1}{2} i \epsilon^{\mu\nu\alpha\beta} q_\alpha p_\beta W_3 + \ldots, \tag{4.6}$$

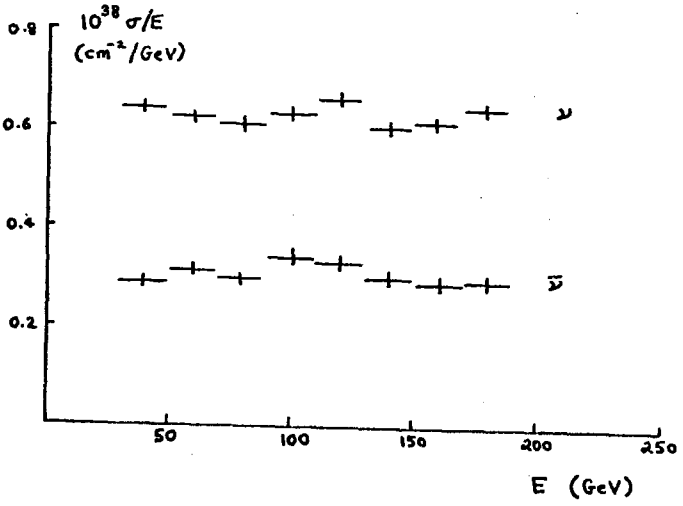

Figure 4.2. σ/E in the two processes (4.1) - data of the CDHS collaboration.

where the terms that I have not written explicitly give contributions that are proportional to the muon mass, and therefore are small, when $W^{\mu\nu}$ is multiplied by $L_{\mu\nu}$. Notice that the structure (4.6) is not identical with (2.3); this is because the weak-interaction current is not conserved, and there is no parity conservation. In the parton model, W_1, W_2 and W_3 are calculated from the diagram of figure 3.1, just as for electron or muon scattering. The only difference is the coupling at the vertex; instead of being determined by the electromagnetic current

$$J^\mu_{EM} = \tfrac{2}{3}\bar{u}\gamma^\mu u - \tfrac{1}{3}\bar{d}\gamma^\mu d - \tfrac{1}{3}\bar{s}\gamma^\mu s \quad (+ c, b, t, \ldots \text{ terms}), \tag{4.7}$$

it corresponds to the charged weak hadronic current

$$J^\mu_{WEAK} = \bar{u}\gamma^\mu(1-\gamma_5)\left[d\cos\theta_c + s\sin\theta_c\right] \quad (+\ldots), \tag{4.8}$$

where θ_c is the Cabibbo angle, $\theta_c \simeq 15°$. If the same valence and sea distributions are used in this calculation as are extracted from e and μ scattering, excellent agreement is obtained with data from ν and $\bar{\nu}$ scattering. As an example, figure 4.3 shows the quark and antiquark distributions required to fit the data from BEBC. Remember

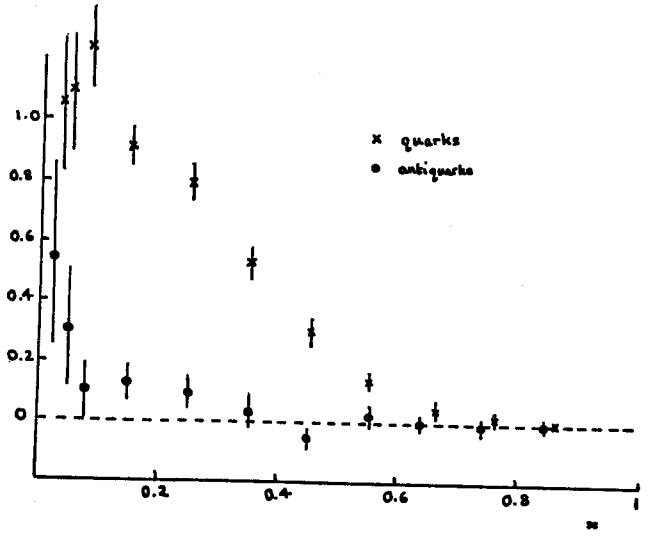

Figure 4.3. Fractional momentum content in the nucleon, as measured at BEBC with $-q^2$ in the range 3 to 100 GeV^2. Notice that the antiquark distribution is entirely nonvalence, while the quarks are a mixture of valence and sea. Compare the curves in figure 3.5 (though note that the normalisation of these is defined differently).

that the antiquarks occur only in the sea, and that the quarks are the sum of valence and sea terms, and compare this figure with figure 3.5.

The data of figure 4.3 are on a heavy liquid target, so that they average the contributions from proton and neutron targets. It is of importance to have more data from hydrogen targets. The reason for this is that if the Bjorken variable x is large enough for the contribution from sea quarks to be negligible, then one can be sure that ν scattering is probing the valence d quark in the proton. (The W^+ is absorbed by the d quark and a u quark is emitted. A u quark cannot absorb the positively charged W. See figure 4.4). Similarly, $\bar{\nu}$ scattering probes

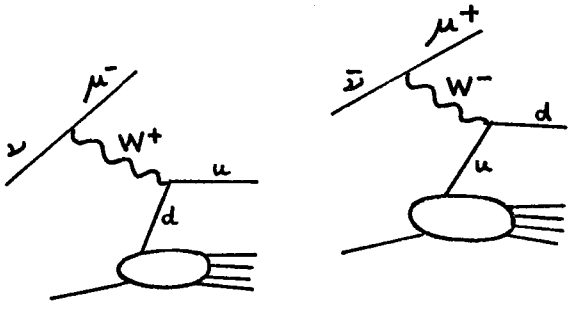

Figure 4.4. Dominant contributions to the processes (4.1) at large values of x.

the valence u quarks. Hence a measurement of the ratio $F_2^{\nu p}/F_2^{\bar{\nu} p}$ at large x gives directly the ratio $d(x)/u(x)$, with no problems about deuterium corrections. In this way, it will be possible to settle thequestion whether this ratio is fixed at 2, or whether it goes to zero as $x \to 1$.

Again, if one wishes to study how a u quark materialises into hadrons after it has been ejected from the proton by the W, one should look at νp reactions at large x. Then, unlike in any other process, one can be sure that the quark being studied is a u rather than, say, a d or a $\bar{u}$. I shall come back to this later.

5. Production of lepton pairs.

One of the most important reactions being actively studied in a number of experiments is

$$pp \to \mu^+\mu^- \text{ (or } e^+e^-\text{)} + \text{hadrons.} \tag{5.1}$$

To lowest order in the electric charge, this occurs through the production of a virtual photon,

$$pp \to \gamma + \text{hadrons,} \tag{5.2}$$

which subsequently decays into the $\mu^+\mu^-$ or e^+e^-. It is important to distinguish between resonance production and continuum production; the two are beautifully illustrated in the famous data of figure 5.1. I first discuss the continuum.

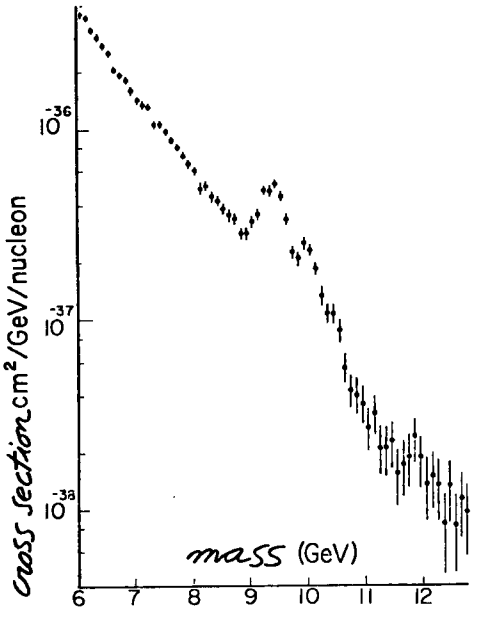

Figure 5.1. Continuum and resonance contributions to the reaction (5.1) - data from the Columbia-Fermilab-Stony Brook collaboration.

Let the 4-momentum of the γ be q, so that $\sqrt{q^2}$ is the invariant mass $M_{\ell\ell}$ of the dilepton system. Now q is timelike, $q^2 > 0$, while in the e, μ and ν scattering processes it was spacelike, $q^2 < 0$. Nevertheless, the parton model allows a calculation of the dilepton production in terms of the quark distributions measured in the scattering processes.

In the centre-of-mass frame, define Feynman's variable

$$x_F = \frac{\text{longitudinal momentum } p_{\parallel} \text{ of the dilepton}}{\text{its maximum possible value}} \qquad (5.3)$$

An alternative to x_F is the rapidity

$$y = \tfrac{1}{2} \log \frac{E + p_{\parallel}}{E - p_{\parallel}}, \qquad (5.4)$$

where E is the energy of the dilepton. This is almost equal to the pseudorapidity

$$\eta = -\log \tan \tfrac{1}{2}\theta, \qquad (5.5)$$

where θ is the centre-of-mass frame angle at which the dilepton (or, equivalently, the virtual photon) emerges. One may choose to work with any one of the three dimensionless variables x_F, y, η, together with another dimensionless variable $\tau = q^2/s$, or $\sqrt{\tau} = M_{\ell\ell} / \sqrt{s}$, where $\sqrt{s}$ is the total centre-of-mass energy.

If there is scaling, so that dependence on fixed dimensional parameters disappears for sufficiently large $M_{\ell\ell}$ and s, then

$$\frac{d^2\sigma}{d\sqrt{\tau}\, dx_F} \text{ or } \frac{d^2\sigma}{d\sqrt{\tau}\, dy} \text{ or } \frac{d^2\sigma}{d\sqrt{\tau}\, d\eta}$$

$$= \frac{1}{M_{\ell\ell}^2} \times \left\{ \begin{array}{l} \text{a dimensionless function of} \\ x_F \text{ or } y \text{ or } \eta \end{array} \right\}. \qquad (5.6)$$

This is tested by the data in figure 5.2. To the extent that the data points lie on a single curve, the scaling is verified.

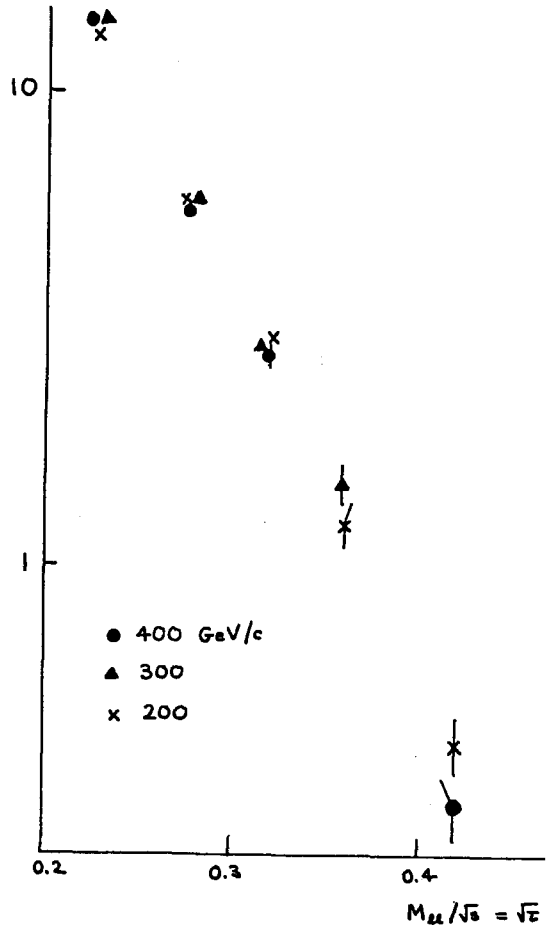

Figure 5.2. Test of scaling of the Drell-Yan continuum in preliminary data from the Columbia-Fermilab-Stony Brook collaboration. The plot is of $M_{\ell\ell}^2\, d^2\sigma / d\sqrt{\tau}\, dy$ at y = 0.2 in proton-nucleus collisions (logarithmic vertical scale).

The Drell-Yan Mechanism.

In the parton model, the virtual photon in (5.2) is produced by the fusion of a quark from one of the initial hadrons with an antiquark from the other. This is the Drell-Yan mechanism, shown in figure 5.3. In this figure, $k_1 \approx x_1 p_1$ and $k_2 \approx x_2 p_2$ - see the discussion

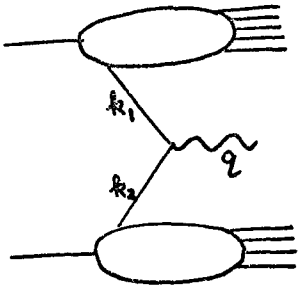

Figure 5.3. The Drell-Yan Mechanism. Additional initial and final state interactions are not shown - see text and figure 5.4.

at the beginning of § 3. Hence $q \approx x_1 p_1 + x_2 p_2$, from which we obtain, asymptotically,

$$x_1 x_2 = \tau = M_{\ell\ell}^2 / s$$
$$x_1 - x_2 = x_F . \qquad (5.7)$$

For given τ and x_F, these equations may be solved so as to determine x_1 and x_2. In particular, when $\theta = 90°$ so that $x_F = 0$, we have $x_1 = x_2 = M_{\ell\ell}/\sqrt{s}$. That is, production of large dilepton masses probes the parton distributions at large fractional momenta x_1 and x_2. Other useful formulae are

$$y = \tfrac{1}{2} \log x_1/x_2$$

$$2E/\sqrt{s} = x_1 + x_2 . \qquad (5.8)$$

Calculation of the Drell-Yan diagram gives

$$\frac{d^2\sigma}{d\sqrt{\tau}\,dy} = \frac{2E}{\sqrt{s}} \frac{d^2\sigma}{d\sqrt{\tau}\,dx_F}$$

$$= \tfrac{1}{3} \frac{8\pi\alpha^2}{3M_{\ell\ell}^2\sqrt{\tau}} F(\sqrt{\tau},\ y \text{ or } x_F), \qquad (5.9a)$$

where, in the same notation as (3.3)

$$F = \sum_{r=u,d,\ldots} Q_r^2 \left[F^{(r)}(x_1) F^{(\bar{r})}(x_2) + F^{(\bar{r})}(x_1) F^{(r)}(x_2)\right]. \qquad (5.9b)$$

The factor $1/3$ in (5.9a) is a consequence of colour: only quarks of the same colour may fuse to form the virtual photon, and there is a 1 in 3 chance of them having the same colour.

It must be mentioned that initial and final state strong interactions modify the simple Drell-Yan diagram of figure 5.3. A final-state interaction is shown in figure 5.4, resulting in the production of additional hadrons. In so far as the "ordinary" strong interactions are concerned, there is a theorem[1] that in the calculation of the inclusive cross-section (5.9), where one is not interested in the final-state hadrons, there is destructive interference and the effects of the initial and final state interactions exactly cancel. That is, one may forget them in the calculation of the inclusive cross-section (5.9), and pretend that only the simple Drell-Yan diagram of figure 5.4 matters. Nevertheless, they do affect the distribution of hadrons in the final state. The theorem applies only to the ordinary strong interactions; there must also be quark-confining interactions if there are to be no fractionally-charged particles in the final state, and the effect of these is, of course, not understood. The hope is that they also can be ignored in the calculation of the inclusive cross-section.

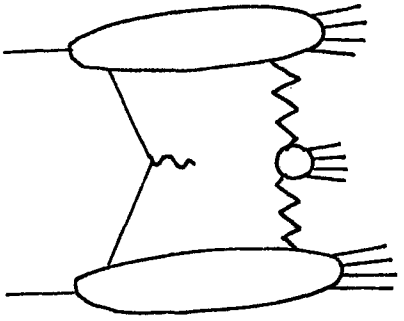

Figure 5.4. A final-state interaction, which modifies the Drell-Yan mechanism.

The Drell-Yan process is of very great importance. One reason is that the antiquark distributions enter multiplicatively in (5.9), so that the cross-section is sensitive to them. Measurements of $d^2\sigma/d\sqrt{\tau}\,dy$ give a more accurate determination of the antiquark distributions than is possible from lepton scattering, where the antiquarks enter additively rather than multiplicatively. Figure 5.5 shows the effect of changing the shape of the antiquark distribution. In comparing data with calculations such as those in figure 5.5, remember that most of the data are for heavy nuclear targets. Experimentally, it seems that cross-sections for massive dilepton production are linear in the mass-number A of the target, but for a heavy target any small discrepancy from this A-dependence can have substantial numerical effect. In any case, there is the additional need to correct the data for the effects of the Fermi motion of the nucleons in the nuclear target, and for secondary interactions. The ultimate test of the Drell-Yan mechanism will be to use a hydrogen target, adjust the parton distributions to give a good fit to the

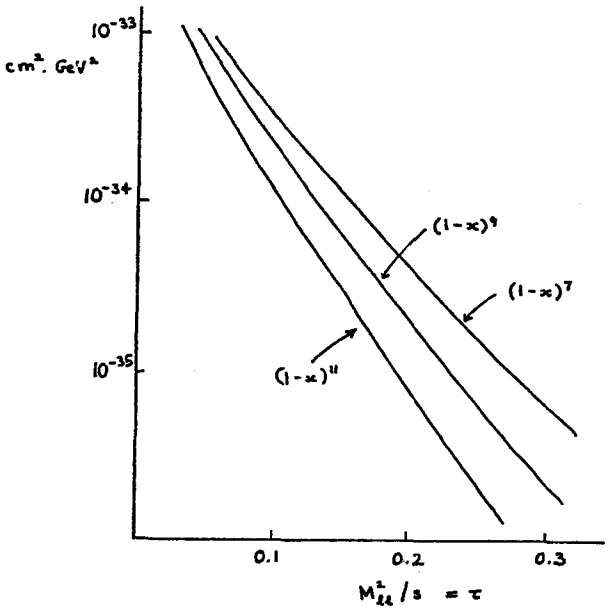

Figure 5.5. The effect on the Drell-Yan calculation of changing the sea distribution in the nucleon (from reference 9). The calculations are for $M_{\ell\ell}^3\, d^2\sigma/dM_{\ell\ell}\, dy$ at $y = 0$.

energy variation of the data at fixed x_F, and then see whether the resulting calculated distributions fit the x_F-dependence at each energy.

Another important feature of the Drell-Yan mechanism is that, by changing to a different beam, one can use it to measure parton distributions in other types of hadron. This is, of course, not possible through lepton scattering experiments. Notice that if the beam is a $\bar{p}$ or a π, the antiquark needed for the fusion can be a valence parton, whereas for a proton beam it has to belong to the sea. Hence when the dilepton mass $M_{\ell\ell}$ is large enough for x_1 and x_2 to be beyond the range of values where the sea distribution is appreciable, one expects that production for $\bar{p}$ or π beams will be rather greater than from a proton beam.

This is verified in the data of figure 5.6, which shows also the results of typical Drell-Yan calculations, including target corrections. For the pion beams, the results of two calculations are shown. The solid curves assume parton distributions in the pion to be not very different from those shown in figure 3.5 for the nucleon; see the solid curves in figure 5.7. The dotted curves assume that the parton distributions in the pion are represented by the dashed curves in figure 5.7, as is proposed by

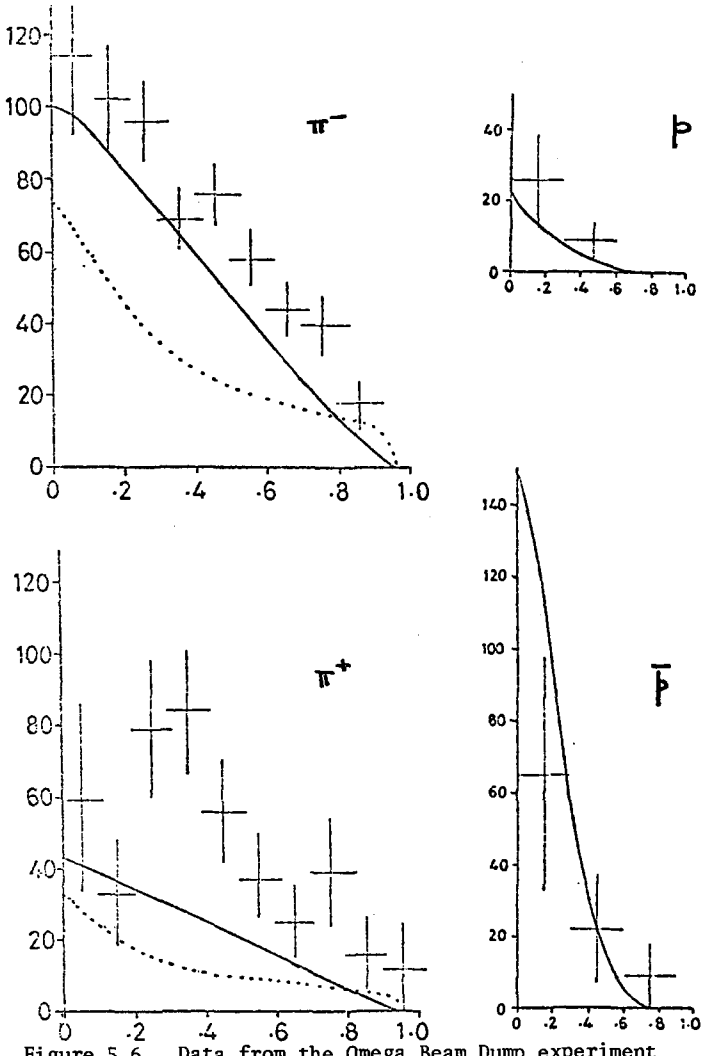

Figure 5.6. Data from the Omega Beam Dump experiment for $d^2\sigma/dM_{\ell\ell}\,dx_F$ (in nb/nucleus / GeV) plotted against x_F for $M_{\ell\ell}$ in the range 1.9 to 2.7 GeV. The different beams are at 40 GeV/c and the target is copper. Calculations by I. Kenyon using the distributions of references 7 (solid curves) and 10 (dotted curves).

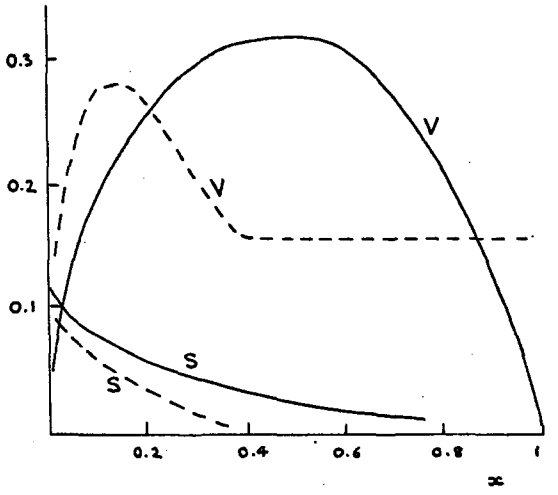

Figure 5.7. Valence and sea distributions in the pion, as proposed in references 7 (solid curves) and 10 (dashed curves).

Feynman and Field[10]. For reasons that I shall return to later, it is of importance to have more dilepton production data from pion beams, in order to determine which type of parton distribution in the pion is more correct.

Comparing production with π^+ and π^- beams gives another useful test of the Drell-Yan mechanism. Suppose that the target has equal numbers of protons and neutrons, for example carbon, so that it contains equal numbers of u and d quarks. Take $M_{\ell\ell}$ large enough to be reasonably sure that contributions from valence partons in both beam and target dominate, so that with a π^+ beam its valence d participates in the fusion, and with a π^- it is the valence u. Then the cross-section ratio at large $M_{\ell\ell}$ should be

$$\frac{\sigma(\pi^+)}{\sigma(\pi^-)} = \left(\frac{\text{charge of } \bar{d}}{\text{charge of } \bar{u}}\right)^2 = \frac{1}{4}. \qquad (5.10)$$

Data for this ratio are shown in figure 5.8. For a hydrogen target, the ratio should be 1/8 if the ratio of the quark distributes u(x) and d(x) in the proton is equal to 2 at large x.

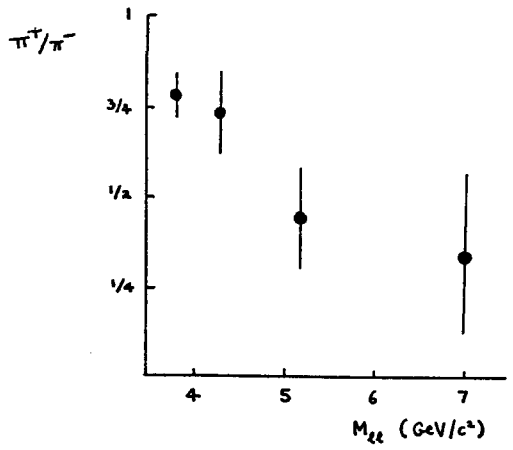

Figure 5.8. Ratio of dimuon production from a carbon target with π^+ and π^- beams (Chicago-Princeton II).

6. W Production.

The Drell-Yan mechanism provides an obvious mechanism for the production of the weak-interaction vector bosons in hadron-hadron collisions. The virtual photon in figure 5.3 is replaced by a $W^{\pm}$ or a Z^0, which now couples to the quarks through the weak current instead of the electromagnetic current. The hope is that the vector boson will be detected through either its leptonic decay, $W \to \mu\nu$ or $Z^0 \to \mu^+\mu^-$, or through its hadronic decays.

In the case of the $W^{\pm}$, the strength of its coupling to quarks is given by (4.4). Gauge theory does not enter into that relation. However, in order to predict the mass M_W, and both the mass and the coupling of the Z^0, it is necessary to assume a specific gauge theory. The Salam-Weinberg model gives[11]

$$M_W = M_Z \cos\theta_W = (\pi\alpha/G\sqrt{2})^{1/2} / \sin\theta_W = (37.5\ \text{GeV}) / \sin\theta_W . \tag{6.1}$$

Here θ_W is the Weinberg angle. Data on neutral-current neutrino reactions find that $\sin\theta_W$ is somewhere between about 0.38 and 0.25, so that M_W is in the region of 60 to 75 GeV, with M_Z a little higher

For W^+ production, the formula analogous to (5.9) is

$$\frac{d\sigma}{dy} = \tfrac{1}{3}\pi G\sqrt{2}\ H(M_W/\sqrt{s},\ y \text{ or } x_F), \tag{6.2a}$$

where

$$H = \left[F^{(u)}(x_1) F^{(\bar{d})}(x_2) + F^{(\bar{d})} F^{(u)}\right] \cos^2\theta_c + \left[F^{(u)} F^{(\bar{s})} + F^{(\bar{s})} F^{(u)}\right] \sin^2\theta_c , \tag{6.2b}$$

with θ_c again the Cabibbo angle. Predictions based on this formula are shown in figure 6.1. W^- and Z_o production may be calculated similarly; the results are not very different.

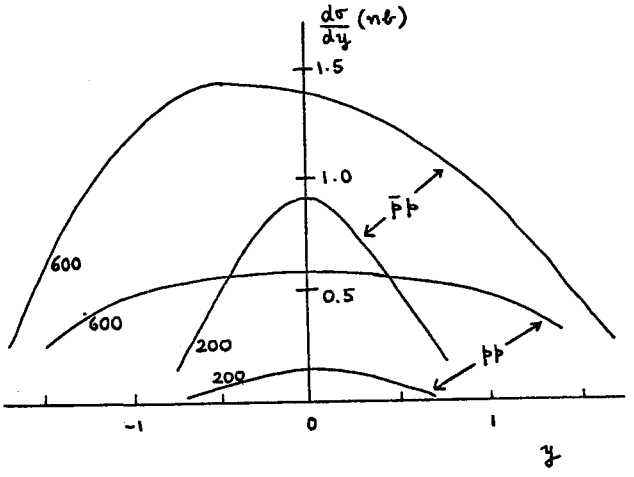

Figure 6.1. Predictions for W^+ production at $\sqrt{s}$ = 200 and 600 GeV (Chase and Stirling).

The cross-sections are expected to be at the nanobarn level, which should give a reasonable production rate in the storage rings now being planned. But it is important to discuss the backgrounds that may obscure the signal; I return to this later.

7. J/ψ and Υ Production.

Mechanisms of the Drell-Yan type have been proposed also for the production of the J/ψ and the Υ in hadronic collisions. There are basically two different types of mechanism. The first is the fusion of ordinary quarks $q\bar{q}$, so as to produce the J/ψ or Υ with a coupling that is Zweig-violating and therefore very small. At least in the case of the J/ψ , the strength of this coupling is calculated from the observed width of the particle, assuming that the hadronic decays occur through a $q\bar{q}$ intermediate state. For $\bar{p}p$ collisions, where the $\bar{q}$ involved in the fusion is necessarily non-valence, the production rate calculated from the mechanism is much less than that which is observed. However, for πp and pp collisions the $\bar{q}$ can be a valence parton of the beam particle, so that at fairly low energy where the fractional momentum x_1 that is required for the q is large the mechanism gives an appreciable contribution. One concludes that at

fairly low energy the cross-section for J/ψ production from $\bar{p}$ and π beams should be rather larger than from a proton beam , as is seen in the data of figure 7.1.

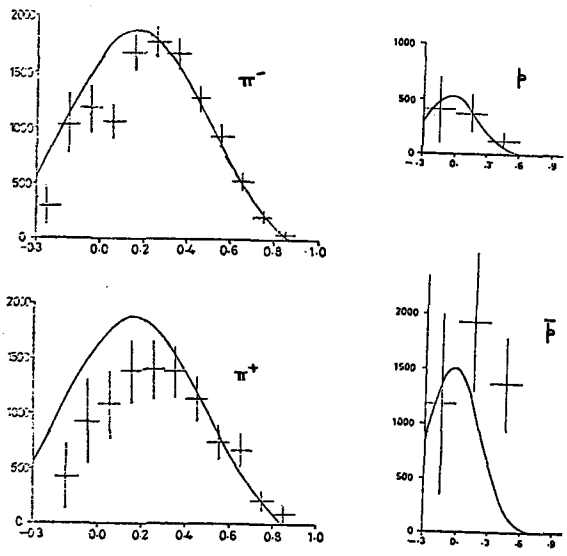

Figure 7.1. Data from the Omega Beam Dump experiment for $d\sigma/dx_F$ (in nb/nucleus) plotted against x_F for J/ψ production with 40 GeV/c beams on a copper target. Calculations by I. Kenyon using the model of reference 7.

The other mechanism, which must also be present in order to explain the data, involves the fusion of a pair of partons whose coupling to the J/ψ or ϒ does not violate Zweig's rule and therefore is larger. However, both partons are non-valence whatever the type of beam, so that the resulting cross-section is only appreciable in magnitude when the energy is so high that the necessary fractional momenta x_1 and x_2 are fairly small (see (5.7)), and the mechanism contributes equal production rates for p and $\bar{p}$ beams. Different authors make different assumptions as to the nature of the fusing partons: in the case of J/ψ production some[7] take them to be $c\bar{c}$ while others[12] take them to be a pair of gluons. In either case the appropriate shape of the parton distribution within the nucleon or pion is chosen by fitting the energy variation of the data; see figure 7.2. The strength of the coupling of the partons to the J/ψ is determined from the normalisation of one of the data points. The x_F dependence of the data at each energy then fits very well to the calculations, as is illustrated in figure 7.1.

It is not known at present which of the two guesses about the nature of the partons in the second mechanism is the right one. The $c\bar{c}$ choice has the

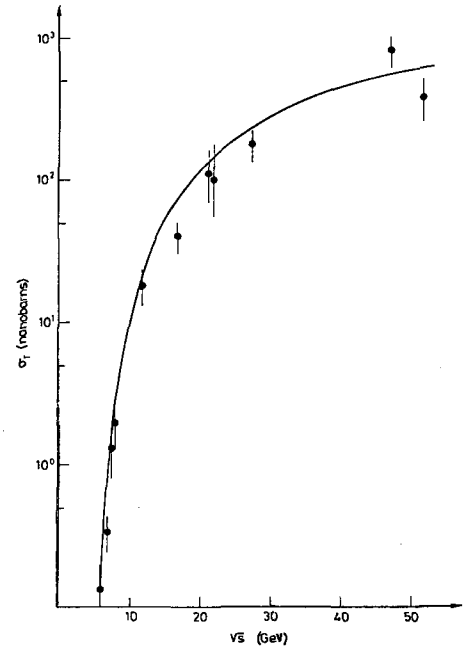

Figure 7.2. Data for pp → J/ψ + X, with calculated curve from reference 7.

apparent problem that, when a charmed quark is pulled out of each beam particle, non-zero charm remains in the residual beam fragments. However, final-state interactions between the two sets of residual fragments can remove the necessity of there being any charmed particles in the final state, particularly at fairly low energies where phase space considerations predict that production of charmed particles in association with the J/ψ is inhibited because of their relatively high mass. No strong experimental evidence for such associated production has been found. In the case of the gg fusion, the system that is produced directly by the fusion has the wrong C-parity. It has to be assumed that this is put right by the radiation of either a photon or a soft gluon, and evidence for the production of photons in association with the J/ψ is indeed found.[13] But it should be noted that the $c\bar{c}$ mechanism can produce states of positive C-parity also.

8. e^+e^- Annihilation.

QED Processes.

The simplest e^+e^- annihilation reaction is $e^+e^- \rightarrow \mu^+\mu^-$. This is a pure QED process, with just one Feynman graph in lowest order (figure 8.1). This graph is easy to calculate, but even without calculation one might guess that, when the energy E of each colliding beam is much greater than the electron mass m_e, the cross-section will not depend on

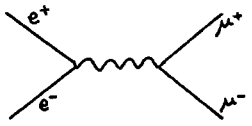

Figure 8.1. Feynman graph for $e^+e^- \to \mu^+\mu^-$.

the masses. Then, from dimensional considerations, $\sigma \sim 1/s$, where $\sqrt{s}$ = 2E is the invariant centre-of-mass energy. Calculation of the Feynman graph gives

$$\sigma \sim \frac{4\pi\alpha^2}{3s}$$

$$\frac{d\sigma}{d\Omega} \propto 1+\cos^2\theta. \qquad (8.1)$$

Another interesting process that is purely a QED process is the two-photon-exchange reaction of figure 8.2, $e^+e^- \longrightarrow e^+e^-e^+e^-$. Evidently, the cross-

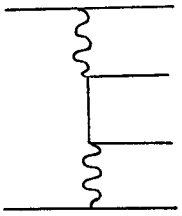

Figure 8.2. Feynman graph for $e^+e^- \longrightarrow e^+e^-e^+e^-$

section for this is proportional to α^4, and therefore it appears to be much smaller than the cross-section (8.1). However, there is a special feature that enhances the contribution from the Feynman graph of figure 8.2. To obtain the cross-section, one integrates over the momenta of the particles in the final state and in this integration the momentum transfers q_1^2 and q_2^2 carried by the two photons vary. At high E, q_1^2 and q_2^2 can take very small values, so that the photon propagators $1/q_1^2$ and $1/q_2^2$ are very large. The result of the integration is that

$$\sigma \propto \frac{\alpha^4}{m_e^2}\left(\log E/m_e\right)^3. \qquad (8.2)$$

Unlike (8.1), this rises with increasing E.

Hadronic Processes.

The two-photon process leads also to hadron production, figure 8.3. The cross-section is cal-

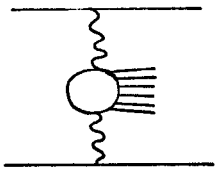

Figure 8.3. Two-photon process leading to hadronic production in the central bubble.

culated in terms of the total cross-section for $\gamma\gamma$ scattering, which may be estimated assuming factorisable pomeron exchange. The conclusion[14] is that even at E = 15 GeV the two-photon process contributes more than 95% of the total e^+e^- cross section. Its cross section rises slowly with increasing energy, unlike the single-photon processes which fall like s^{-1}, and so its relative importance rises very rapidly with increasing E. Notice that, because the dominant contribution arises from small momentum transfers q_1^2 and q_2^2, where the photons move in a direction almost parallel to the incoming beams, nearly all the hadrons are produced close to the beam directions. However, the chance of there being hadrons produced with large transverse momentum is not negligible[14].

Most of the interest in hadron production from e^+e^- colliding beams lies in the one-photon process. In the parton model, this corresponds to a diagram just like figure 8.1, but with the $\mu^+\mu^-$ replaced by a quark-antiquark pair. There has to be some final-state interaction if there are to be no fractionally-charged particles in the final state, but it is assumed that there is unit probability of this occurring, so that the cross-section is calculated just from the $e^+e^- \to q\bar{q}$ part of the reaction. Because of the similarity of the coupling of the photon to $\mu^+\mu^-$ and $q\bar{q}$, the prediction then is that

$$R = \frac{\sigma(e^+e^- \to \text{hadrons})}{\sigma(e^+e^- \to \mu^+\mu^-)} = 3\sum_{r=u,d,\ldots} Q_r^2, \qquad (8.3)$$

where, as usual, Q_r is the charge carried by the quark of flavour r. The factor of 3 occurs if each flavour is found in three colours. For r = u, d, s the prediction (8.3) is R = 2, while if c is added R rises to 10/3. Data from both SPEAR and PLUTO find

that, below the charm threshold, R is just a little greater than 2. Above the charm threshold and the various structures associated with it, PLUTO finds a value for R quite close to 10/3, while SPEAR finds it to be about one unit higher.

Jets.

After the q and the $\bar{q}$ have been produced, each materialises as a jet of hadrons. It is assumed that the quark-confining interaction between these two jets substantially affects only their slowest component particles. Since the e^+e^- annihilation occurs in the centre-of-mass frame, the intermediate virtual photon is at rest, and so the pair of jets emerges back-to-back in any direction. At fairly low beam energies E, the axis that defines the jet direction is not immediately evident from inspection of the event, and it has to be found by a sphericity analysis. This analysis amounts to guessing an axis, calculating the sum over all the particles of the square of the momentum component $p_\perp$ transverse to the axis and varying the direction of the axis until this quantity is minimised. Distributions of $p_\perp$ relative to the axis so chosen are shown in figure 8.4. Notice

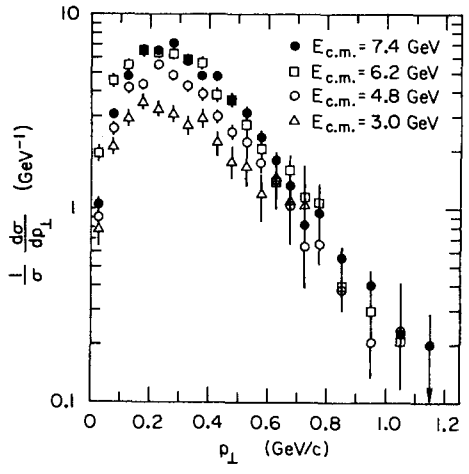

Figure 8.4. Distribution of momentum components perpendicular to jet axis in e^+e^- annihilation (reference 15).

that $\langle p_\perp \rangle$ remains close to about 300 MeV/c even at large energy.

This, then, is the operational definition of a jet, as deduced from experimental data: a jet is a collection of particles whose momentum component perpendicular to their total momentum vector is limited to a few hundred MeV/c. When the total momentum of the jet is 2.5 GeV/c, on average one finds two charged particles and one neutral; at 5 GeV/c these average multiplicities are nearly doubled. Combining these pieces of information, one can sketch scale plan drawings of typical jets, as I have done in figure 8.5. These jets do not look very jet-like,

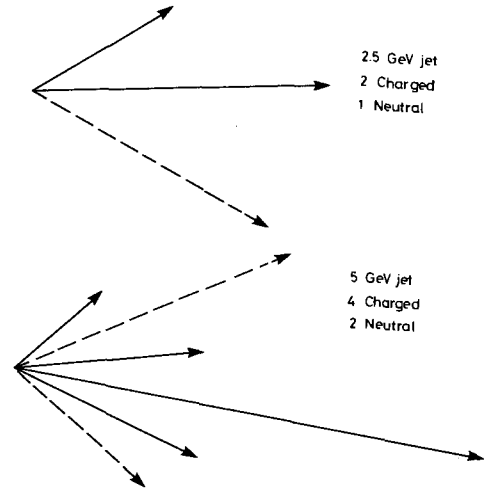

Figure 8.5. Scale drawings of "typical" jets; the dashed lines represent neutral particles.

which is why at low energies the sphericity analysis is needed to reveal their presence. However, as the energy increases the jet structure begins to become apparent to the naked eye; figure 8.6 shows an exam-

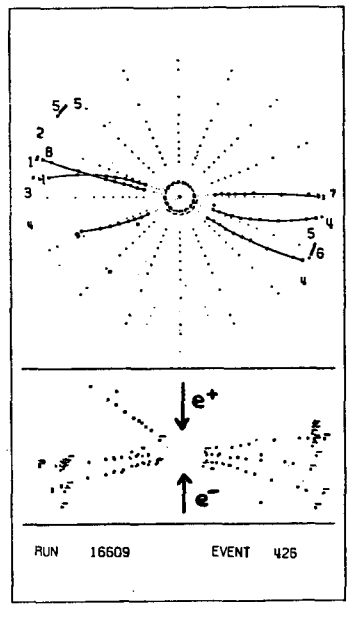

Figure 8.6. A pair of jets from PLUTO. Each jet has E = 4.68 GeV; only charged particles are seen.

le of a not untypical event at energy 2E = 9.35 GeV.

When the jet axis has been determined from event to event, one can ask what is its angular dist-

ribution relative to the initial e^+e^- beam directions when the events are summed. Because the virtual photon has spin 1, the answer must be of the form $1 + \lambda \cos^2\theta$, for some λ. If the jets each have spin $\frac{1}{2}$, then $\lambda = 1$ as in (8.1). For spin 0, $\lambda = -1$. The data give[15] $\lambda = 0.97 \pm 0.14$, in agreement with the expected value for quarks.

A distribution of some importance is that of z, where z is the fractional longitudinal momentum of the component particles in the jet. Data from PLUTO are shown in figure 8.7, which indicates also the

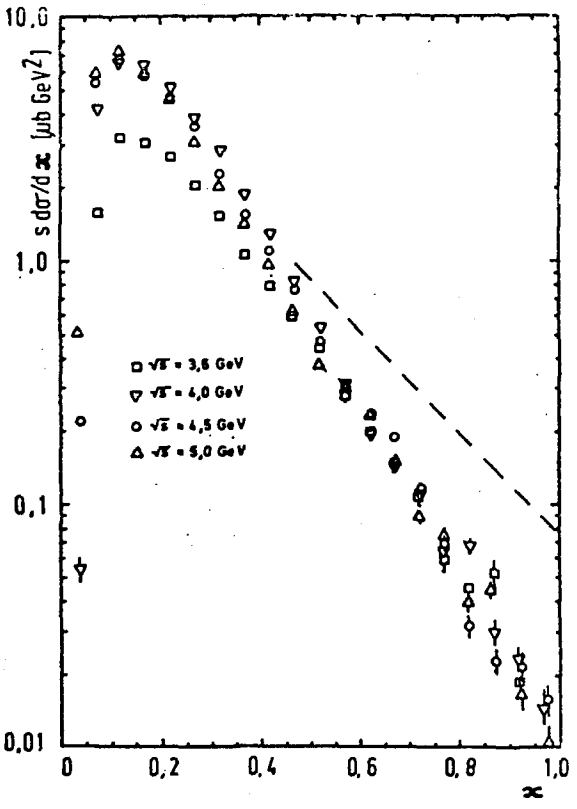

Figure 8.7. Momentum distribution of charged hadrons at PLUTO. The dashed line indicates corresponding data from SPEAR. The distribution shown here is in $x = 2p/\sqrt{s}$; that in z is similar.

results from SPEAR. Notice that to a good approximation there is scaling: the z-distribution varies little with energy. Most of the jet components are pions, particularly at large values of z. It is expected that the quark fragmentation into pions near z = 1 is directly related to the distribution of quarks within a pion near x = 1. In particular, if one goes to a non-zero constant, so should the other. Hence the SPEAR data would favour the dashed curve in figure 5.7 for the valence parton distribution in the pion, while the PLUTO data would favour the solid curve in the latter figure. I shall return to this later.

In deep inelastic e, μ or ν scattering, the parton that absorbs the virtual γ or W is ejected and materialises as a jet: see figure 3.2. This jet is expected to be similar to those found in e^+e^- annihilation. Superficially, such a similarity is indeed found, but more exact experimental comparison is needed.

Quark Jet Fragmentation.

There is a widely-held belief that when a quark fragments to form a jet of hadrons, the fastest hadron tends to be such that it contains the quark as a valence quark. For example, a u-quark jet commonly contains a fast π^+, π^0 or K^+, but more rarely a fast π^- or K^-. The best way to investigate this belief experimentally is in ν and $\bar{\nu}$ interactions on a hydrogen target. I explained that then, when ω is not large, the flavour of the emerging quark is known. The available data support the belief, but more investigation is needed.

The question has been studied theoretically in a cascade model[16]. Consider, for definiteness, the pair of jets produced in e^+e^- annihilation. As the q and $\bar{q}$ separate, a colour field is set up between them. It is assumed that this field is such that the energy contained in it increases as the q and $\bar{q}$ separate, so that new $q\bar{q}$ pairs are created in the field. The fragmenting quark meets an antiquark belonging to a pair formed in this way, and fuses with it to form a meson. The quark that originally belonged to the pair then continues on in more or less the direction of the initial quark, until it in turn meets an antiquark. The process repeats itself until almost all the energy is shed, and the remaining quark is so slow that it readily fuses with a slow antiquark arising elsewhere in the reaction. See figure 8.8. The first meson produced in the cas-

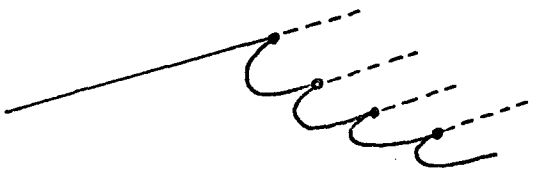

Figure 8.8. Cascade model for fragmention of a quark into mesons. Eventually, a slow quark remains, which annihilates with a slow antiquark from elsewhere in the reaction.

cade process evidently does contain the original quark as a valence quark, but it is not always the

fastest meson. Again, the first meson produced may be an unstable one, and its decay products can then be slower than some of the other mesons produced further down the chain. So in this model the retention of quantum numbers by the fastest hadron in the jet is not perfect, though it does occur approximately.

9. Exclusive Processes at Large t.

Deep inelastic processes involving leptons are associated with a γ or W that has very short wavelength. This therefore probes the short-distance structure of the hadrons and that is why the reaction mechanisms have the simplicity displayed by the parton model. Purely hadronic reactions in most cases are not associated with short-distance effects: when two protons collide, their collision is usually a glancing one which involves only their outer structure. It is not clear whether the parton model has anything simple to say about such collisions, though there is a possibility that it may, as I shall discuss later. Rather rarely, however, two protons will collide head-on, so that then the interaction does directly involve their short-distance structure and it may be hoped to have a simple parton-model description. The way to pick out the events in which there has been a head-on collision is to study those that contain a large momentum transfer.

I consider first the exclusive processes at large t:

$$A + B \to C + D . \tag{9.1}$$

Although the theoretical understanding of these is not as well-based as in the case of leptonic processes, there is fairly good reason to suppose that, at least to a good approximation, the large-t differential cross-section should take the form

$$\frac{d\sigma}{dt} \sim s^{-m} F(\theta). \tag{9.2}$$

Here θ is the centre-of-mass scattering angle and the parameter m is fixed. It has been proposed that there is a simple rule[8] that predicts the value of m:

$$m = n_A + n_B + n_C + n_D - 2, \tag{9.3}$$

where n_H is the number of valence partons in hadron H. This rule is called the dimensional counting rule. For pp elastic scattering at large t, the rule predicts m = 10. This is well satisfied by data at PS energies, for $-t \gtrsim 2.5$ GeV^2, as is shown in figure 9.1. In that figure, the straight lines actually

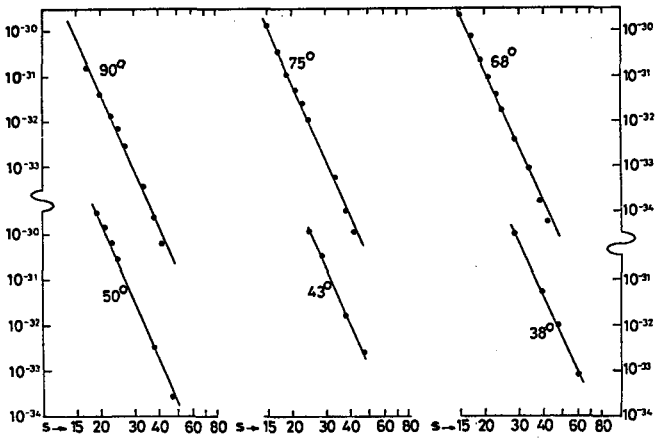

Figure 9.1. pp elastic scattering data at PS energies. The straight lines correspond to (9.2) with m = 9.7.

correspond to m = 9.7. In will be interesting to have good data for other types of beam, to check whether m changes according to the prediction (9.3).

Figure 9.1 shows data only at PS energies. If one plots the energy dependence of $d\sigma/dt$ at fixed t, as in figure 9.2, one sees that over the PS energy

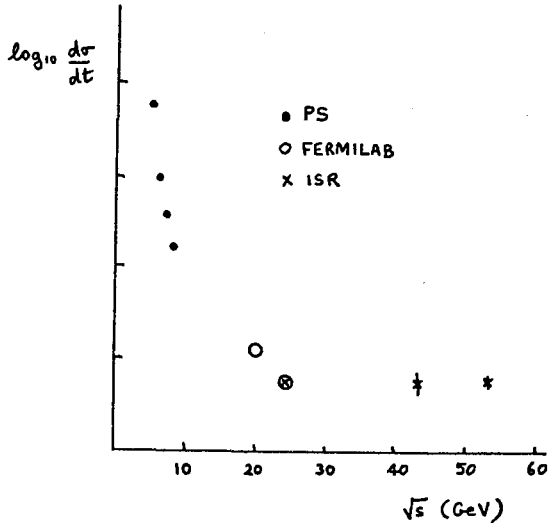

Figure 9.2. pp elastic scattering data at $-t = 6$ GeV^2 (reference 17).

range it falls sharply. Data from Fermilab find that the fall-off has become more gentle, while over the IRS energy range there is no detectable energy variation at all. This suggests that a new dynamical mechanism may have become dominant at very high energy.

A concrete realisation of the dimensional-counting result, m = 10, is provided[8] by the constituent-interchange diagram of figure 9.3a. Here, the prot-

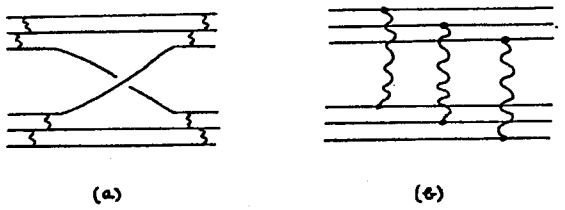

Figure 9.3. Models for large t elastic pp scattering: (a) constituent interchange; (b) multiple scattering.

ons consist of three quarks, bound together by gluon exchange, and they interact by interchanging a quark between them. It has been known for some time[18] that a different kind of mechanism gives instead m = 8, so that at any fixed θ it should dominate over the constituent-interchange mechanism when the energy becomes large enough. This mechanism is shown in figure 9.3b: each quark in one proton scatters at the same angle θ on one of the quarks in the other, so that after the scatterings the three components of each proton are again moving together in a new direction and can readily re-combine. If the wide-angle scatterings occur through the exchange of a spin-one gluon, and if $-t$ is large but $\ll s$, one finds that figure 9.3b gives

$$\frac{d\sigma}{dt} \sim t^{-8}. \tag{9.4}$$

This is independent of s, as are the ISR data. It is compared with the t-dependence of the data in figure 9.4.

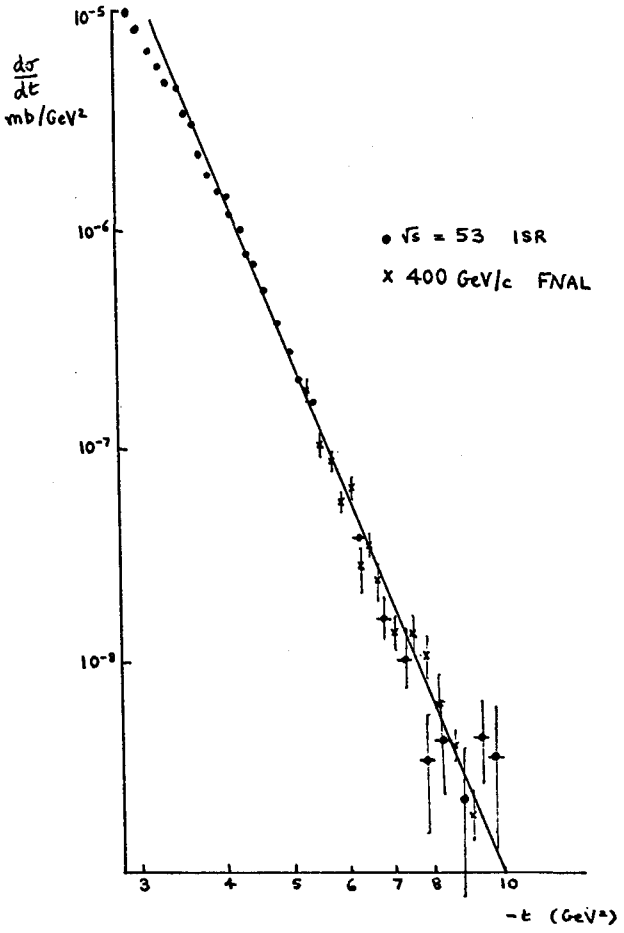

Figure 9.4. pp elastic scattering data from CERN-Hamburg-Heidelberg-Annecy-Vienna and Cornell-McGill-Northeastern-Lebedev. The straight line corresponds to t^{-8}.

10. Inclusive Processes at Large Transverse Momentum.

Consider the inclusive production of pions at 90°:

$$pp \to \pi X. \tag{10.1}$$

In the typical reaction, where the protons have only glancing collision, the pion has only small transverse momentum. At small p_T, the spectrum falls sharply with increasing p_T:

$$E\frac{d\sigma}{d^3p} \sim e^{-6p_T}, \tag{10.2}$$

and it varies rather slowly with energy. However, for $p_T \gtrsim$ 1 GeV/c, when presumably the proton-proton collision is more head-on, the spectrum is found to fall much less sharply and at a fixed value of p_T there is a marked rise with increasing energy. This is seen in the early data of figure 10.1, which shows also the extrapolation of the exponential fit (10.2) to small-p_T data.

The dynamics of small-p_T hadronic reactions is complicated, but the change in the character of the spectrum at large p_T encourages the hope that there a new and simple dynamics has set in. It is usual to introduce the dimensionless variable

$$x_T = 2p_T/\sqrt{s}, \tag{10.3}$$

together with the centre-of-mass angle θ at which the pion is produced. Then if there is scaling, in the sense that there is no dependence on any fixed dimensional parameter, one expects

$$E\frac{d\sigma}{d^3p} \sim p_T^{-n} F(x_T, \theta) \tag{10.4}$$

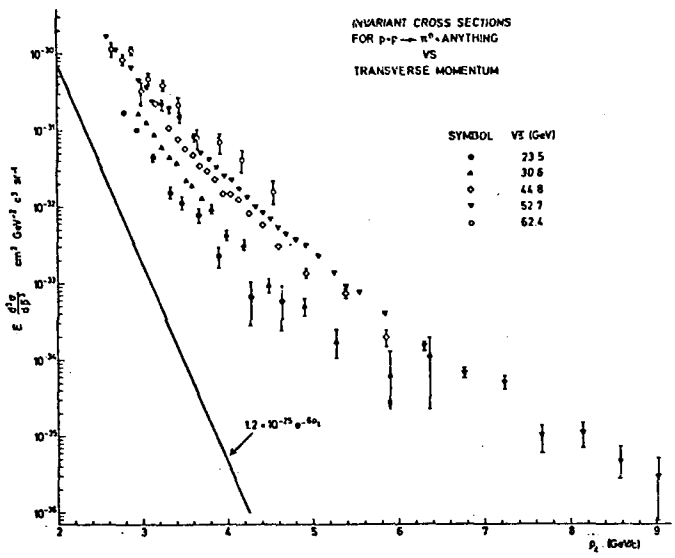

Figure 10.1. Early data from CERN-Columbia-Rockerfeller for π^0 production at 90°. The straight line is an extrapolation of the data at small p_T .

with n = 4. This does not fit existing data. However, the data do fit the form (10.4) with n = 8, so that the function F carries dimensions and therefore contains some fixed dimensional parameter. This is shown in figure 10.2, where it is seen that the

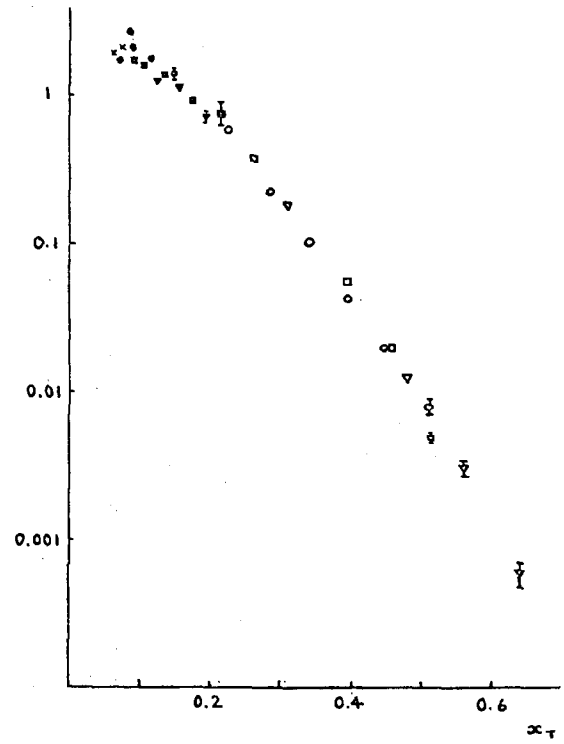

Figure 10.2. p_T^8 E dσ/d^3p for $pp \to \pi^+ X$ at 90°. The upper points are from the British-Scandinavian experiment at the ISR, and the lower ones are from the Chicago-Princeton experiment at Fermilab.

θ = 90° data for p_T^8 E dσ/d^3p , when plotted against x_T, lie on a single curve for a wide range of energies. It is widely believed that experiments at large values of p_T and s may show that an n = 4 term is also present. There is a hint that this may be so in recent data at very large p_T from the ISR, but the situation is far from clear-cut and it will be of great interest to explore it further in the new colliding-beam facilities that are being planned.

Most of the recent experimental work on large-p_T processes, particularly at the CERN ISR, has been concerned with the study of correlations[2]. It has been found that large-p_T events contain an interesting jet structure.

In the ordinary, low p_T events the final-state particles are found to emerge in two jets, one in the direction of each of the colliding beams. In the large-p_T events, these longitudinal "beam fragment" jets are still present, but there are in addition two transverse jets. One of these contains the high-p_T particle used to trigger the detection apparatus. The transverse momentum of the jet on the other side approximately balances that of the trigger-side jet, but it emerges in a different direction from event to event. The characteristic four-jet structure is shown in figure 10.3.

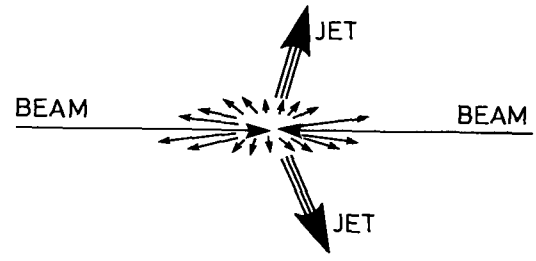

Figure 10.3. Four-jet structure in high-p_T events. The two transverse jets have been exaggerated in this figure. The longitudinal jets are apparently similar to those seen in low-p_T events.

Figure 10.4 shows some of the data that verify the existence of the opposite side jet. These data are obtained with a 90° trigger pion, having p_T in the range 2.5 to 4.5 GeV/c. They plot the rapidity difference Δy between pairs of away-side particles, for those events in which there are at least two such particles having $p_T > 800$ MeV/c. This restriction is imposed in order to reduce the possibility that the two particles belong not to the away-side transverse jet but instead to one of the two longitudinal jets. This possible confusion always exists and adds to the difficulty of disentangling the final-

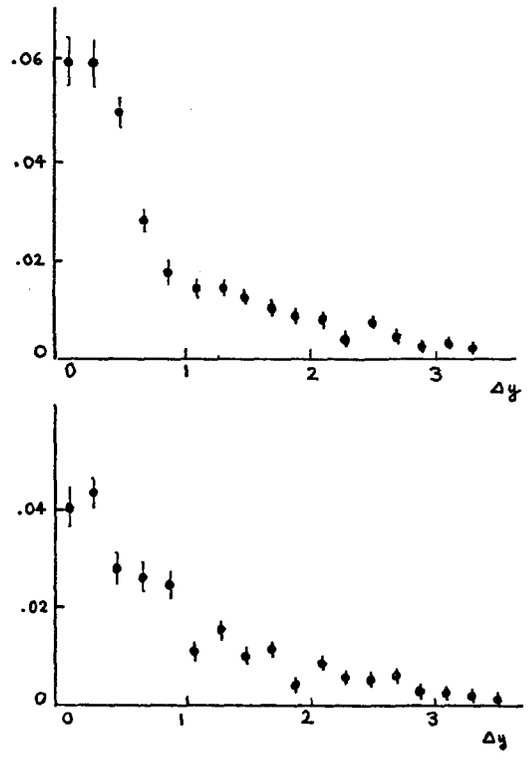

Figure 10.4. Distribution of rapidity difference Δy of two particles having $p_T > 800$ MeV/c opposite a high p_T trigger pion at 90° (British-French-Scandinavian).

state structure, but it should be reduced when higher trigger p_T values can be achieved. The clear peak seen in the Δy distribution at small values of Δy, both for the case where the two particles have opposite charge and when they have the same charge, is the evidence for the presence of the away-side jet. It is not clear whether the points having large Δy correspond to events where one of the two particles still belongs to one of the longitudinal jets, or whether they indicate the presence of some other structure. But at least it is seen that a single away-side transverse jet is a prominent feature of the data.

The trigger-side jet.

Most of the large-p_T experiments so far have triggered on a single high-p_T particle. This means that the trigger selects the special class of high-p_T events where the trigger-side jet gives most of its momentum to one particle, the trigger particle. Normally, a jet does not choose to fragment into hadrons in this way; its momentum is shared more equally among the particles. That is, if one uses a calorimeter trigger and demands a certain p_T in the calorimeter, so that one is triggering on a jet rather than a single particle, most of the events will not contain any one particle that has particularly large p_T. Because the single-particle trigger biases towards the selection of rather unusual events, it reduces the magnitude of the cross-section. From a simple study of correlation data from the ISR it was predicted that the cross-section for a calorimeter trigger set at a given value of p_T should be some 2 orders of magnitude greater than for a single particle of the same p_T. This appears to have been verified in recent experiments at Fermilab, and so the use of calorimeter triggers is likely in the future to make possible the study of events in which the total p_T is much higher than up to now. The main difficulty will be to design the calorimeter so as to accept the whole of the transverse jet, and only the transverse jet.

With a single-particle trigger, most of the trigger-side jet momentum is usually given to the trigger particle. But occasionally this is not so, and there is a second fast particle in the trigger-side jet. With a trigger π^0, a fast π^+ or π^- is sometimes found, and plots of the invariant mass of the pair of pions show a clear ρ signal. From this, it is deduced that production of a ρ with a given p_T is comparable with that of a single pion having the same p_T. However, it is far from true that the trigger-side jet structure is fully described by the ρ : one also finds strong correlations between pairs of π^0, or pairs of pions of the same charge. In fact, in the literature there are two main alternative suggestions as to the identity of the trigger-side jet: (i) it is a fragmenting quark, like an e^+e^- jet, and (ii) it is a $q\bar{q}$ system, that is either a π, a ρ, an ω, and higher meson systems, with also perhaps a $q\bar{q}$ continuum.

It is not yet known whether either of these two suggestions is correct. However, there is one problem with the suggestion that the trigger-side jet is a fragmenting quark. This is a measurement of the total momentum in the trigger-side jet. In order to understand this[2], let us use the following approximate parametrisation of the cross-section for the production of a jet of large transverse momentum (integrated over the angle of production):

$$\frac{d\sigma}{dP_T} = \frac{A}{P_T^{n-1}} \cdot \qquad (10.5)$$

It is found that with this parametrisation, A and n

are only slowly varying with p_T when the energy is fixed. Assume that the jet fragmentation function scales, as is approximately found in the e^+e^- data of figure 8.7. That is, the probability F(z)dz of finding a hadron whose fractional longitudinal momentum is in the range z to z + dz is a function of z only. Then the cross-section for production of a particle with large transverse momentum p_T is

$$\frac{d\sigma}{dp_T} = \int_{p_T}^{\infty} dP_T \frac{A}{P_T^{n-1}} \int dz\, F(z)\, \delta(p_T - zP_T)$$

$$= \frac{A}{p_T^{n-1}} \int dz\, z^{n-2} F(z). \qquad (10.6)$$

This result has two interesting features. First, the powers of p_T and P_T are the same; this is the parent-child-relation[19]. Secondly, the data show that n is large, $n \gtrsim 10$, so that the factor z^{n-2} in the integral means that values of z close to 1 dominate in the integration. This is just the trigger-bias effect: most of the jet momentum is given to the trigger particle. The average total momentum in the jet is calculated by including an extra factor P_T under the integral (10.6):

$$\langle P_T \rangle = \frac{\int dP_T\, P_T \frac{A}{P_T^{n-1}} \int dz\, F(z)\, \delta(p_T - zP_T)}{d\sigma/dp_T} \qquad (10.7)$$

If the jet is similar to the e^+e^- jet, this can be calculated from the data for F(z) in figure 8.7. The SPEAR data, where F(z) is constant as $z \to 1$, give an answer close to $1.2\, p_T$, while the DESY data rather give an answer closer to $1.5\, p_T$. If, on the other hand, the jet is a $q\bar{q}$ system, any value is possible, because we have no advance knowledge of the relative importance of the different components π, ρ, ω, ... Figure 10.5 shows data for the total momentum of the charged particles accompanying a trigger particle of transverse momentum p_T, approximately within a cone of half-angle 45° surrounding the trigger particle. The straight-line fit is drawn because (10.7) predicts that $\langle P_T \rangle \propto p_T$. Some of the detected momentum corresponds to particles that do not belong to the trigger jet, but rather to the background contributed by the two longitudinal jets. As is indicated in figure 10.5, it is assumed that the contribution from this background varies little with the trigger p_T. After correcting for acceptance and for the undetected neutrals, the conclusion then is that $\langle P_T \rangle < 1.1\, p_T$. Hence the proposal that the jet is similar to an e^+e^- jet is not favoured, even if it is not correct to assume that the background is not constant. However, this needs more study and it would be premature to reach a firm conclusion.

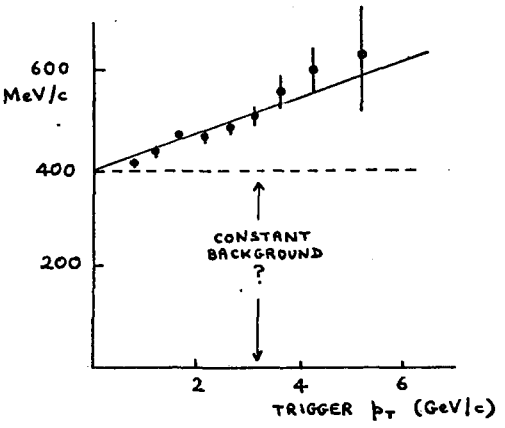

Figure 10.5. Total momentum of charged particles accompanying trigger particle (British-French-Scandinavian).

Hard-Scattering Models.

Most of the theoretical study of large p_T inclusive processes nowadays is within the framework of hard-scattering models, figure 10.6. In a sense, the statement that a hard-scattering model is appropriate

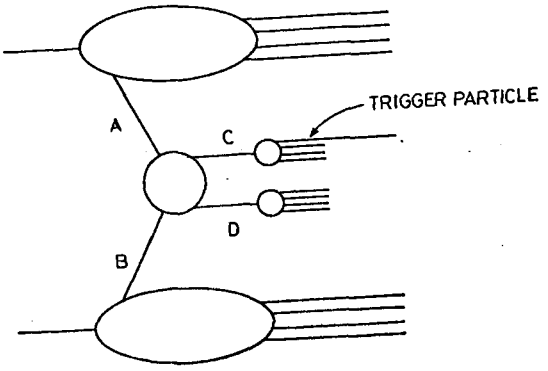

Figure 10.6. The hard-scattering mechanism.

is directly equivalent to the statement that the final state has the four-jet structure shown in figure 10.3. The transverse jets of figure 10.3 are the objects C and D of figure 10.6, and if these are to emerge with large transverse momentum they must have been produced through a wide-angle scattering of some constituent A of one incoming particle on some constituent B of the other. The central question, *whose answer we do not yet know*, is what are A, B, C and D?

If one makes the simplest assumptions, the calculation of figure 10.6 leads to an inclusive cross-

section having the structure (10.4). I shall discuss later how these assumptions might be modified, so that a different result is obtained. If one uses the dimensional-counting rule (9.2) and (9.3) for the central wide-angle scattering, one obtains

$$\begin{aligned} qq \to qq,\ qg \to qg,\ gg \to gg \text{ etc} \quad & n = 4 \\ q\bar{q} \to MM,\ qM \to qM \quad & n = 8, \end{aligned} \tag{10.8}$$

where g denotes a gluon and M a $q\bar{q}$ system. The data strongly favour n = 8, but I shall explain later how perhaps the processes that give n = 4 with the simple assumptions might be adapted so as to come closer to the data. The interest in this is that these processes are all associated with quantum chromodynamics in a direct way.

11. The Longitudinal Jets.

The large p_T event structure of figure 10.3 contains a pair of longitudinal beam-fragmentation jets, in addition to the transverse jets. A pair of beam-fragmentation jets is a feature also of small-p_T processes. Because such processes do not involve any hard scattering, it in not clear whether they have any simple parton-model description. However, the literature contains several apparently very successful calculations of beam fragmentation in parton-model pictures, so that even if we are not able to give these calculations any fundamental justification they are worth considering seriously.

Perhaps the most obvious calculation does not work: it gives too few fast hadrons, compared with experimental data. In this approach, the quarks are supposed to be distributed in the beam particle with the longitudinal momentum distributions measured in deep inelastic lepton scattering, and they then fragment into hadrons with the fragmentation functions measured in e^+e^- annihilation. The literature[20] contains two apparently different modifications of this approach. Each seems rather successful, but they cannot both be correct.

In the first picture, the quark again fragments as in e^+e^- annihilation, but instead of being given a variable fractional longitudinal momentum within the beam particle it is assumed to take almost all its momentum. The excuse for this assumption is that then the other constituents of the beam particle must be moving rather slowly, and this is said to be necessary in order that there may be an appreciable interaction with the target. In the second picture, the quark is given the longitudinal momentum distribution within the beam particle as measured in lepton scattering, but it does not fragment. Rather, it annihilates with a slow antiquark produced in some other part of the interaction.

12. Backgrounds in W Production.

Figure 12.1 shows data for the production of

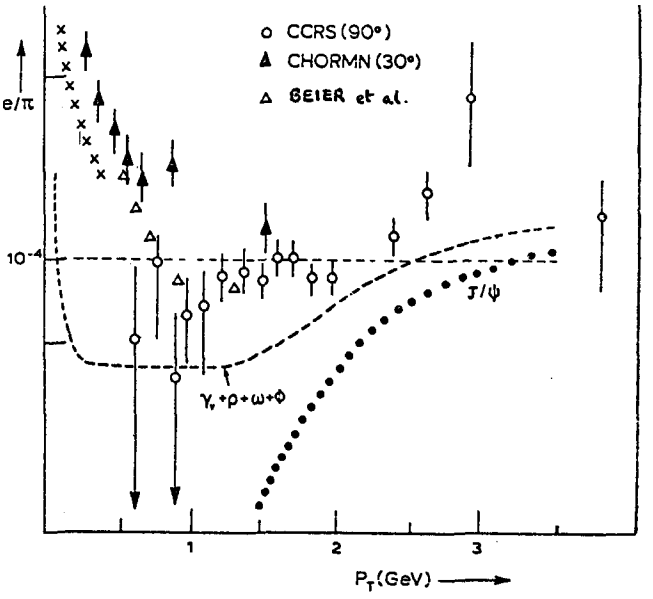

Figure 12.1. "Direct" electron production. The curves show contributions from various sources (reference 19).

direct electron production (with contributions from decay of pions subtracted out), compared with production of pions at the same transverse momentum. As is indicated in the figure, these electrons are thought to be produced from a variety of sources, mostly rather uninteresting ones. It is not clear whether there is also a substantial signal from some more interesting origin, such as charmed-particle production. The ratio e/π is seen to be at the 10^{-4} level, and this is found to be the case also for the ratio μ/π. The direct muon production will provide a background in experiments that aim to detect the W through its decay $W \to \mu\nu$.

The W is expected to decay through the simple vertex Feynman graph of figure 12.2. The coupling at the vertex is g, given in(4.4), and the fermion lines are $\mu\nu$ for the leptonic decay (or $e\nu$), and a quark-antiquark pair in the case of a hadronic decay. Each diagram gives a readily calculable contribution to the width of the W, so the partial width into any channel is known, but the total number of channels available for W decay is not known. Considering only

$\mu\nu$, $e\nu$ and four quark flavours gives

$$\frac{\Gamma(\mu\nu)}{\Gamma_{total}} = \frac{1}{8}, \qquad (12.1)$$

but this estimate omits the heavy lepton τ, the new quark that constitutes the Υ, and all the other new quark flavours that will surely be found to have mass less than $\frac{1}{2} M_W$, that is less than 30 to 40 GeV. So the estimate (12.1) could well be too large by a factor of 2 or more.

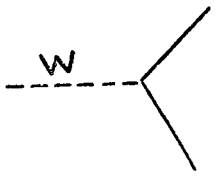

Figure 2.2. W decay; the coupling is either to leptons or to quarks.

Using the branching ratio (12.1) and convoluting the $W \to \mu\nu$ decay distribution with a W production calculation such as is shown in figure 6.1, the muon signal at 90° is as is shown in figure 12.3. There

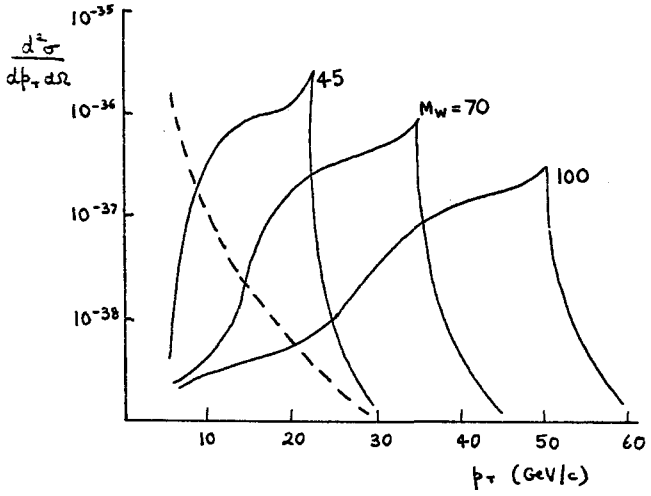

Figure 12.3. Production of muons at 90° via a W, for three possible values of M_W, in pp collisions at $\sqrt{s}$ = 400 GeV. The dashed curve represents the estimated background from direct muons (reference 21).

is a peak at $p_T = \frac{1}{2} M_W$; the shape of the rise to this peak is determined mainly by the longitudinal momentum distribution of the W predicted from the Drell-Yan production mechanism, while the right-hand side of the peak has a fall-off largely determined by the total width of the W. If the total width is twice as much as is assumed in (12.1), the peak in figure 12.3 is correspondingly wider and ¼ the height.

The calculation has included no transverse momentum for the W; there might well be several GeV/c of transverse momentum, which would smudge out the peak. The dotted line in figure 12.3 is an estimate of the background from direct muon production, assuming that μ/π remains at about 10^{-4} and making what is in this context the most pessimistic prediction about pion production at these large values of p_T and s, namely that the value of n in (10.4) has changed to 4. Figure 12.3 encourages the hope that the W may be readily detectable from the muon signal alone; if it is not, things can be improved by using a hadron calorimeter opposite to the muon detector, so as to pick out those events where the large transverse momentum of the muon is balanced on the other side by an undetected neutrino instead of the hadron jet expected in the case of the background muons.

In the case of the hadronic decays of the W, the quarks in figure 12.2 fragment into hadrons and a pair of jets is expected exactly similar to those seen in e^+e^- annihilation. However, from what we know about jet production in ordinary large p_T reactions it is expected that the background of jets will swamp the signal from the W, even if n = 4 in (10.4) has not yet been reached. But perhaps it will be possible to establish the presence of the W from a peak in the invariant mass distribution of the combined pair of transverse jets.

13. Breaking of Bjorken Scaling.

In the various reactions that I have discussed, scaling seems to be a remarkably good feature of the data. Nevertheless, there are clear deviations from scaling, as is seen in the deep inelastic muon and neutrino scattering data shown in figures 2.3 and 13.1. At small x, F_2 rises slowly with increasing $-q^2$, while at large x it falls.

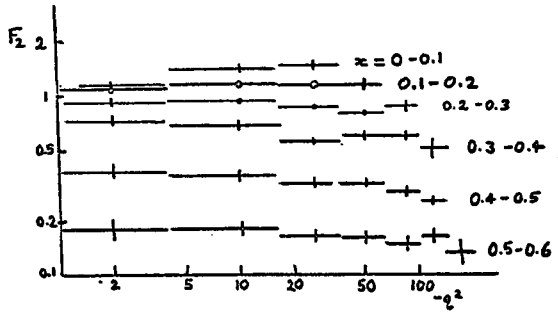

Figure 13.1. Measurements of $F_2(x,q^2)$ in neutrino scattering (CDHS collaboration).

Mass Effects.

A large part of the deviations from scaling is due to parton mass effects. As I shall now explain, unfortunately we do not know how to calculate these mass effects at all exactly, so that we cannot be sure how much of the breaking of scaling has a more interesting dynamical origin.

Consider the simple parton model that eventually is supposed to scale at large enough values of ν and $-q^2$ (figure 13.2). The question that must be

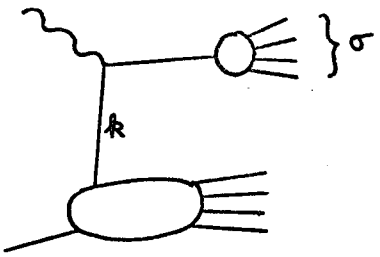

Figure 13.2. Quark parton model for deep inelastic scattering. σ is the squared invariant mass of the quark jet before the confining force begins to act.

answered is how this scaling is approached, so that one needs to calculate the next-to-leading order contribution, which contributes terms of order ν^{-1} to $F_2(x)$. It is found[22] that, correct to terms of order ν^{-1}, the contribution from figure 13.2 is found essentially by replacing x by

$$\xi = x + \frac{\langle\sigma\rangle - x^2M^2}{2\nu}, \qquad (13.1)$$

where M is the mass of the target hadron and $\langle\sigma\rangle$ is the average value of the squared invariant mass of the quark jet. That is, F_2 is constant at fixed ξ. Notice that this result is correct only up to terms in ν^{-1}, which may not be good enough for a completely accurate analysis of present data. But there is a more serious problem that it takes account only of the impulse-approximation contribution of figure 13.2. In the scaling parton model, this contribution is the only one that survives in the ultimate scaling limit, and in leading order it satisfies the current-conservation conditions $q_\mu W^{\mu\nu} = W^{\mu\nu} q_\nu = 0$. But in non-leading orders it does not, so that in non-leading orders there must be contributions from other, more complicated diagrams. We have no idea of how to calculate these.

If we assume that nevertheless the variable ξ provides at least an approximate description of the mass effects, we explain a large part of the deviations from scaling. Notice that we must consider the contribution from each quark flavour separately, because $\langle\sigma\rangle$ varies with the flavour. We do not understand the effects of the quark-confining forces, but presumably $\langle\sigma\rangle$ describes the mass of the fragmenting quark before the confining force has had a chance to act, and so for u and d quarks it is less than $(350\ \mathrm{MeV})^2$. These quarks dominate F_2 for x large, where only the valence contributions matter. Hence for large x, $\xi \lesssim x - x^2M^2/2\nu$. So if F_2 is fixed ξ, the large x part of the plot of F_2 against x approaches the ultimate scaling curve from the left as ν or $-q^2$ increases. Taking account of the shape of the curve, this means that, at fixed large x, F_2 decreases with increasing $-q^2$. As we have seen in figures 2.4 and 13.1, the data do show a decrease of F_2 at fixed large x. Near x = 0, $\xi \lesssim x + \langle\sigma\rangle/2\nu$, so that the variation is in the opposite direction, as also is seen in the data. The variation resulting from heavy quarks can be particularly rapid, until values of $\nu \gg$ their squared mass $\langle\sigma\rangle$ are reached. It is an interesting question how much of the rise seen at small x is due to the contribution from charmed quarks. Notice that a charmed quark may contribute to F_2 without any charmed particles appearing in the final state; just as the final-state interaction that must be added to figure 13.1 anihilates fractional charge, so also it may annihilate charm. Indeed, there is a kinematic incentive for it to do so, until ν becomes very large, because charmed particles are relatively massive.

QCD Effects.

Once the mass effects are subtracted out (if only we knew how to do this), the remaining scale-breaking is interpreted as coming about because the wavelength of the virtual photon decreases as $-q^2$ increases, and so structure in the partons themselves is progressively revealed.

A concrete model in which this occurs is provided by quantum chromodynamics[5]. Rather as in quantum electrodynamics the force is transmitted by the spin-one photon, in QCD it is transmitted by the spin-one gluon. However, while the photon couples to charge but itself carries no charge, the gluon couples to colour and does carry colour. Consequently, in QCD there is a three-gluon vertex which has no analogue in QED, so that there are vital differences between the two theories.

The theory contains a bare coupling between gluons and quarks, figure 13.3a. This is dressed by various insertions; some of the lowest-order ones are shown in figure 13.3b. The various terms must be

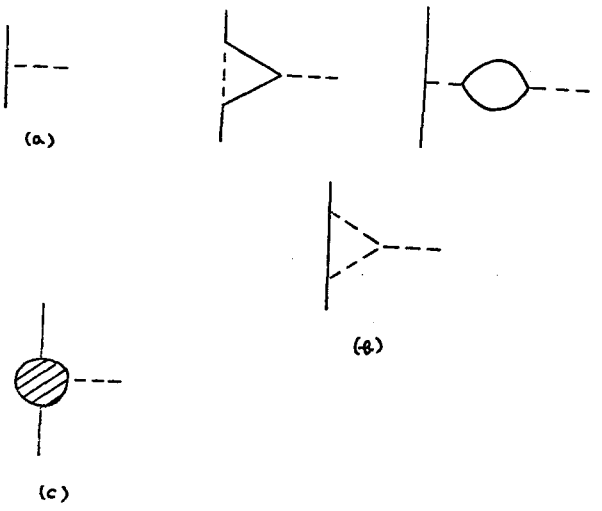

Figure 13.3. The quark-gluon vertex: a) the bare vertex, b) some lowest-order corrections to it, c) the complete vertex.

summed and then the sum is renormalised, resulting in an effective strong-interaction "fine-structure constant" α_s, figure 13.3c, that varies when the squared mass of any of its three legs is varied. Because of the presence in figure 13.3b of the term that contains the three-gluon coupling, α_s decreases to zero when any of its legs is taken far off shell. For this reason, the theory is said to be "asymptotically free". Legs being far off shell correspond to interactions at short distance, and the smallness of α_s in this situation allows the strong-interaction effects at short distance to be calculated in perturbation theory.

A quark may radiate a gluon, which then fragments to form a jet of hadrons. In deep inelastic e or μ scattering, this may happen before the quark absorbs the virtual photon, as in figure 13.4a. This

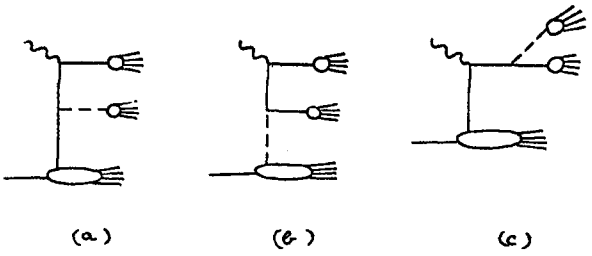

Figure 13.4. Low-order QCD corrections to figure 13.2.

means that the fractional momentum probed by the photon is reduced, some of it having already been radiated away by the gluon. So the curve $F_2(x)$ is shifted to the left in the x plot , and the more so the larger the value of $-q^2$. Once again, the effect at fixed large x is to decrease F_2 with increasing $-q^2$. Another possible QCD effect is shown in figure 13.4b. Here a gluon constituent of the target hadron couples to a quark-antiquark pair. Because the gluon has zero charge, it cannot absorb the virtual photon directly, but the photon can couple to the $q\bar{q}$ pair. This pair production occurs mainly at small values of x, and there it produces a rise in F_2 as $-q^2$ increases.

Another QCD effect is that a quark may radiate a gluon before it fragments to form a jet of hadrons. This can occur in deep inelastic scattering, as shown in figure 13.4c. It turns out that the interference between this diagram and that of figure 13.4a also contributes to the breaking of scaling. The radiation of a gluon before the quark fragments can also occur in the e^+e^- annihilation diagram, as in figure 13.5a.

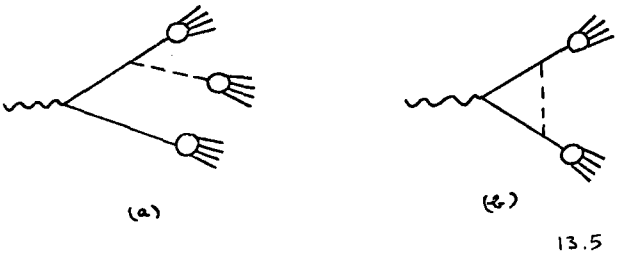

Figure 13.5. Corrections to the simple parton model for e^+e^- annihilation.

Another QCD modification to the basic parton e^+e^- mechanism involves an internal virtual gluon, shown in figure 13.5b. This gives a modification to the ratio R of (8.3), which to lowest order in α_s becomes, up to some theoretical uncertainties,

$$\frac{\sigma(e^+e^- \to \text{hadrons})}{\sigma(e^+e^- \to \mu^+\mu^-)} = 3\sum_{r=u,d,\ldots} Q_r^2 \left(1+\frac{\alpha_s}{\pi}\right). \qquad (13.2)$$

The expression for α_s obtained from a sum of diagrams such as is shown in figure 13.3, and subsequent renormalisation, is

$$\alpha_s = \frac{12\pi}{25 \log Q^2/\Lambda^2}. \qquad (13.3)$$

Here Q^2 is the squared 4-momentum of whichever leg in the diagram of figure 13.3c is being taken off-shell, and Λ is a parameter that cannot be calculated. It would be helpful to have a direct physical interpretation of the mass-scale set by Λ (or the length-scale set by Λ^{-1}), but none seems to have been given yet. It is usually supposed that $\Lambda \approx 500$ MeV. This

comes from fits to the scale-breaking in deep inelastic e or μ scattering. However, because of the problem of how correctly to allow for the mass effects, and because, particularly at small x, the scale breaking obtained from the diagrams of figure 13.4 is sensitive to the shape of the unknown distribution of gluons in the hadron, this value for Λ cannot be accepted as final. Figure 13.6 illustrates the results of one particular calculation of F_2. With Λ = 500 MeV, $\alpha_s \approx 1/3$ in the range 10 GeV$^2 < Q^2 <$ 50 GeV^2, so that $\alpha_s / \pi \approx 10\%$ and the QCD effect in (13.2) is actually rather small.

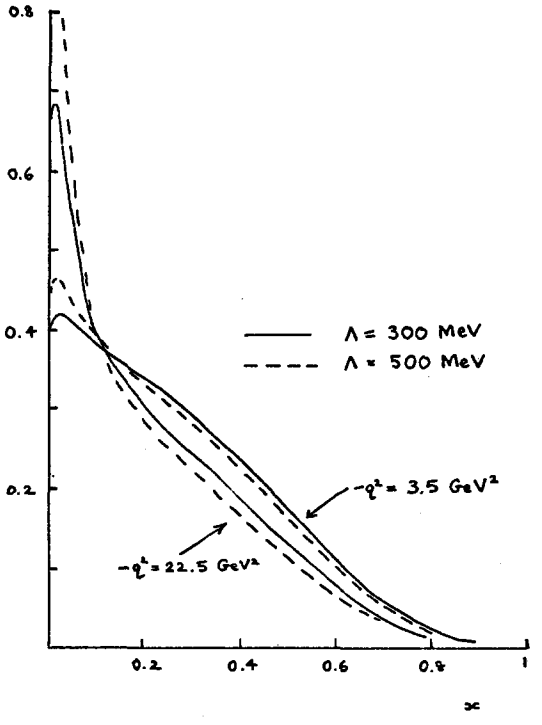

Figure 13.6. The effect of QCD corrections to $F_2(x,q^2)$. At small x the curves are sensitive to the shape of the unknown distribution of gluons in the proton. (Reference 23).

Notice that, except in deep inelastic scattering where there is an alternative, operator formalism not based directly on individual perturbation-theory diagrams, there is always a problem in how to identify Q^2 with the external variables in a reaction. Theoretical manipulations work to leading order in logarithms, and the problem is that to leading order one has, for example $\log Q^2 = \log \frac{1}{2} Q^2 = \log (Q^2 + \text{const.})$. Thus while in e^+e^- annihilation it seems rather natural to identify $Q^2 = s$, the theoretical work cannot show that it should not rather be, say, $Q^2 = \frac{1}{2} s$. Asymptotically it makes no difference but at present values of s it does matter which choice is made.

Drell-Yan in QCD.

The Drell-Yan formula (5.9) was initially derived assuming that the parton distributions scale and so are functions of x only. If the e or μ scattering experiments find that there is also a variation with q^2, one might guess that this variation should be reflected in (5.9). In deep inelastic scattering, q^2 is a momentum transfer and so $q^2 < 0$, while in the Drell-Yan process the large variable is $M_{\ell\ell}^2 > 0$. Perhaps the obvious guess is to insert into the Drell-Yan formula the deep inelastic scattering data obtained at $q^2 = -M_{\ell\ell}^2$. In so far as the QCD effects are concerned, this has been verified to lowest order in α_s and to leading order in logarithms. So again there is the problem whether one should not really have for example $q^2 = -\frac{1}{2} M_{\ell\ell}^2$, or some other choice that is equivalent to leading order in logarithm. Asymptotically it makes no difference, but at presently accessible values of $M_{\ell\ell}$ the different choices do give large numerical differences. In addition, the mass effects in deep inelastic scattering and the Drell-Yan process are certainly different, but cannot really be calculated in either case. Figure 13.7,

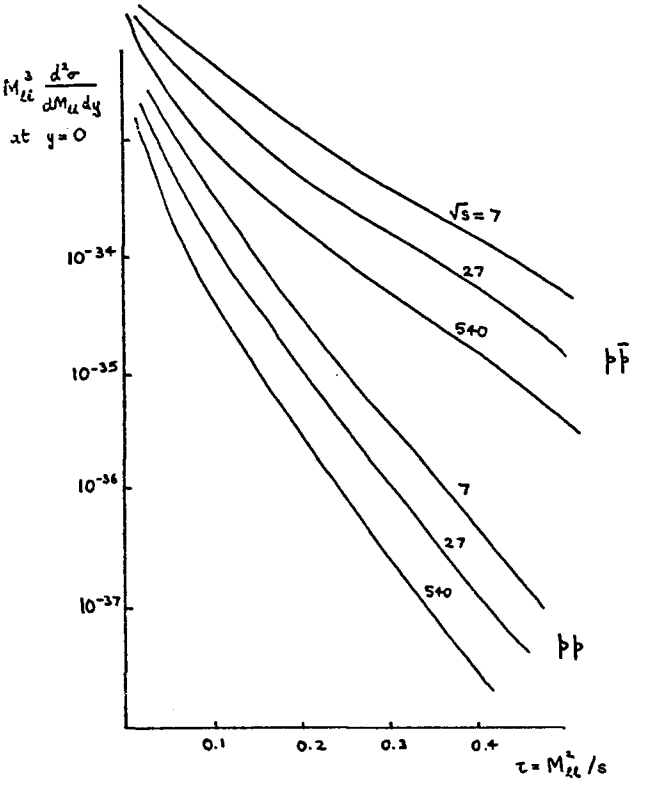

Figure 13.7. Predictions for scale-breaking effects in continuum dilepton production (reference 24).

which shows predictions for scale-breaking in the Drell-Yan process, should be viewed with these difficulties in mind.

14. The Transverse Momentum of Partons.

The transverse momentum of large-$M_{\ell\ell}$ lepton pairs produced in proton-nucleus collisions is measured to be surprisingly large: see figure 14.1. The transverse momentum of the dilepton is equal to that of the virtual photon. In the Drell-Yan mechanism, this is in turn equal to the sum of the transverse momenta of the quark and antiquark that fuse to form the photon. Since the sum here is a vector sum, $\underset{\sim}{q}_T = \underset{\sim}{k}_{T1} + \underset{\sim}{k}_{T2}$, and the relative orientation of $\underset{\sim}{k}_{T1}$ and $\underset{\sim}{k}_{T2}$ is presumably random, one has $\langle q_T^2 \rangle = \langle k_{T1}^2 \rangle + \langle k_{T2}^2 \rangle$. Assuming that the average transverse momenta of the quark and the antiquark are equal, each must therefore be equal to $\langle q_T \rangle / \sqrt{2} \approx 850$ MeV/c.

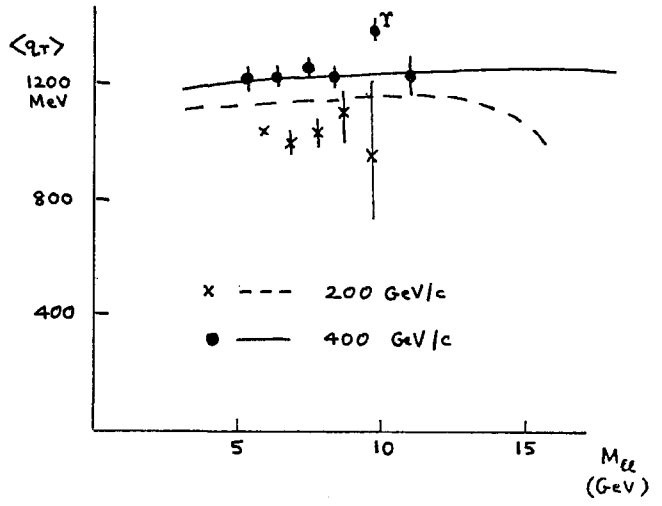

Figure 14.1. Average transverse momentum of dileptons produced in proton-nucleus collisions. Data from Columbia-Fermilab-Stony Brook, calculations from reference 24

Part of this transverse momentum can originate from the QCD effects shown in figure 14.2. In these diagrams, the large q_T of the dilepton is balanced, at least partly, by a gluon jet or a quark jet recoiling with transverse momentum in the opposite direction. Calculations find that the observed $\langle q_T \rangle$ is too large for all of it to be balanced by the recoiling quark or gluon jets. That is, the quark or gluon constituents in the hadron wave function must have some "primordial" transverse momentum before the QCD effects occur. It is not known how large this primordial component should be expected to be. It probably varies with the fractional longitudinal momentum x of the constituent. One does not really know how to combine it with the transverse momentum generated by the QCD effects; the calculations shown in figure 14.1 simply add on a constant 500 MeV/c to the QCD-generated contributions.

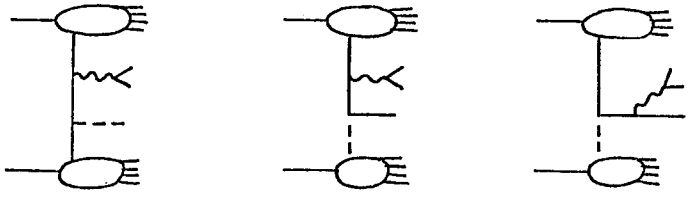

Figure 14.2. QCD corrections to Drell-Yan mechanism.

This is a rather typical problem encountered in trying to compare the predictions of QCD with experiment. Although asymptotic freedom makes it possible to calculate the short-distance effects in a strong interaction by perturbation theory, in most cases there are parts of any reaction that do not depend on short-distance structure. These cannot be calculated by perturbation theory, and their effects can well swamp the ones that can be calculated.

15. QCD and Large p_T.

In the hard scattering diagram of figure 10.6, an obvious choice for the central wide-angle scattering is qq → qq. If it is assumed (i) that this occurs through the exchange of a single gluon with constant coupling, (ii) that the distributions of quarks in the initial hadrons scale, (iii) that the fragmentation functions of the quarks into hadrons scale, and (iv) that the quarks have negligible transverse momentum before they scatter each other, one obtains (10.4) with n = 4. If each of the assumptions (i) to (iv) is relaxed, the qq scattering diagram provides a much better fit to the data, which prefer the value n = 8.

With present knowledge, relaxing each of the four assumptions introduces a considerable amount of arbitrariness into the calculation. It has been shown[25] that in QCD the assumptions (i), (ii) and (iii) should be modified so that the constant coupling of the gluon is replaced by the "running" coupling (13.3), and the quark distributions and fragmentation functions should be replaced by the non-scaling ones as measured in lepton scattering and e^+e^- annihilation. (In the latter case, the break-

ing of scaling is predicted but not yet seen.) There are the usual problems about mass effects and how to identify Q^2 with the variables in the diagram. When the modifications to the assumptions (i) and (iii) are made, the contribution from the mechanism no longer takes the simple form (10.4) with a fixed value of n. However, it is useful to talk in terms of the resulting effective value of n. According to the calculations of Field[25], using the running coupling changes n from 4 to 4.9, introducing breaking of scaling into the quark distributions changes n from 4.9 to 5.2, and breaking the scaling of the quark fragmentation changes n from 5.2 to 5.9.

In the framework of the hard-scattering model, the large-p_T cross-section is small because the central wide-angle scattering cross-section is small. However, if the constitutents A and B in figure 10.6 have transverse momentum before the scattering, and if this is aligned towards the trigger, the central scattering does not have to be through such a wide angle and so the magnitude of the cross-section is enhanced. Field finds that putting in an average transverse momentum of 850 MeV/c for each quark before the scattering changes the effective value of n from 5.7 to 7.1. Further, the calculated magnitude of the cross-section then fits data well for $p_T \gtrsim 6$ GeV/c.

To improve the fit for smaller values of p_T, contributions from other choices for the central scattering are included. In QCD, natural choices are $qg \rightarrow qg$, $gg \rightarrow gg$, $q\bar{q} \rightarrow gg$ and vice versa, where g denotes a gluon. Expected sizes for different contributions are shown in figure 15.1. When all the contributions are added together, agreement with the data is surprisingly good, though certainly not perfect. However, I must stress again that there are several arbitrary ingredients in the calculation.

Finally, I mention direct photon production at large p_T (that is, photons that do not come from the decay of a π^0 or other particle). In QCD, this can be calculated from the diagrams of figure 14.2 by replacing the virtual photon with its attached leptons by a real, high p_T photon. Predictions are shown in figure 15.2, together with a representation of data for π^0 production. The γ production is expected to be rather large. Similar predictions have been made in some other models; see for example figure 15.3. The "data" in that figure should probably be interpreted as upper limits, because of the great difficulty of the experiment.

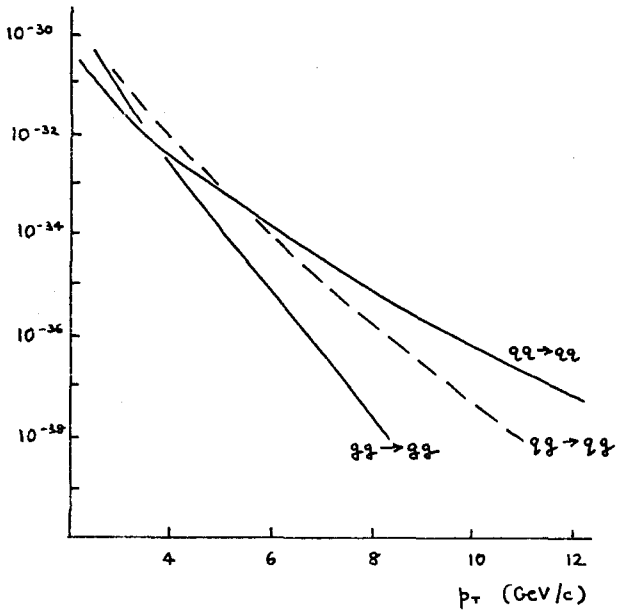

Figure 15.1. Contributions of different hard scatterings to 90° pion production at $\sqrt{s}$ = 53 GeV (reference 27).

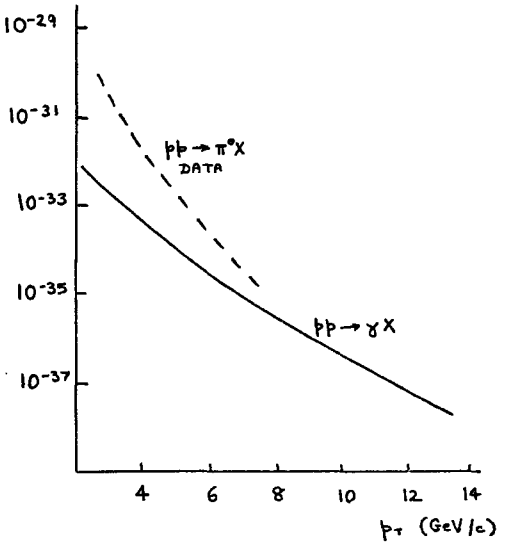

Figure 15.2. QCD predictions for direct photon production at 90° with $\sqrt{s}$ = 53 GeV, and data for π^0 production (reference 24).

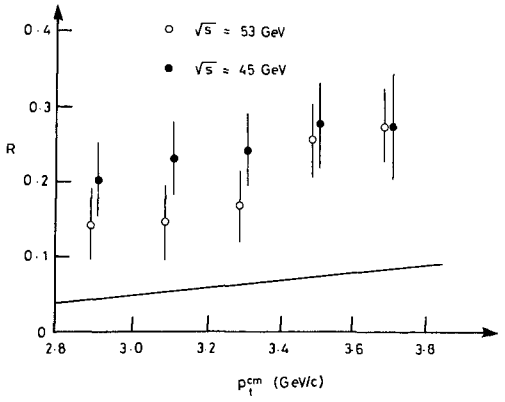

Figure 15.3. Direct photon production. Data from CERN 412, prediction from reference 28.

16. Conclusions.

The most striking feature of the quark parton model is how well it seems to agree with experiment, even in its simplest version. It is important to try and achieve understanding of quark confinement, and of its effects on the structure of final states, but it seems that these effects may be fairly simple.

Quantum chromodynamics provides the only full field theory of strong interactions available at present, and the immediate future will see much work towards trying to establish its connection with experiment. This is not straightforward, because only certain quantities in the theory may be calculated in perturbation theory, and it is not easy in the data to separate these from those that can not be calculated. However, with a theory that makes predictions for such a wide range of different reactions there is the exciting prospect that, by working closely together, experimentalists and theorists can gradually piece together a complete picture of interactions at high energy and short distance.

References.

This list contains mostly review articles, which should be consulted for references to the original papers.

1) P.V. Landshoff and H. Osborn, in Electromagnetic Interactions of Hadrons, ed. Donnachie and Shaw (Plenum).

2) M. Jacob and P.V. Landshoff, Physics Reports, to be published.

3) L.M. Hand, review talk at 1977 International Symposium on Lepton and Photon Interactions at High Energies, Hamburg.

4) W.B. Atwood et al., Phys. Lett. 64B, 479 (1976)

5) W. Marciano and H. Pagels, Physics Reports 36C, 139 (1978).

6) P.V. Landshoff and J.C. Polkinghorne, Phys. Rev., to be published.

7) A. Donnachie and P.V. Landshoff, Nuclear Physics B112, 233 (1976) and Manchester preprint.

8) D.I. Sivers, S.J. Brodsky and R. Blankenbecler, Physics Reports 23C, 1 (1976).

9) L.M. Lederman, Cargèse lectures (1977).

10) R.D. Field and R.P. Feynman, Phys. Rev. D15, 2590 (1977).

11) J.C. Taylor, Gauge Theories of Weak Interactions (Cambridge University Press).

12) J.R. Ellis, Comments on Nuclear and Particle Physics, to be published.

13) J.H. Cobb et al., Phys. Lett. 72B, 497 (1978).

14) S.J. Brodsky, T.A. DeGrand, J.F. Gunion and J.H. Weis, SLAC-PUB-2102.

15) G. Hanson, 7th International Colloquium on Multiparticle Reactions, Tutzing (1976).

16) L. Sehgal, review talk at 1977 International Symposium on Lepton and Photon Interactions at High Energies, Hamburg.

17) K. Winter, review talk at European Conference on Particle Physics, Budapest (1977).

18) P.V. Landshoff, rapporteur talk at XVII International Conference on High Energy Physics, London (1974).

19) N.S. Craigie, Phys. Reports, to be published.

20) W. Ochs, Nuclear Physics B118, 394 (1977); B. Andersson, G. Gustafson and C. Peterson, Phys. Lett. 71B, 337 (1977); K.P. Das and R.C. Hwa, Phys. Lett. 68B, 459 (1977); D.W. Duke and F.E. Taylor, Fermilab preprint 77/95; Phys. Rev. D17. 1788 (1978); S. Pokorski and L. Van Hove; CERN TH 2427; F.C. Erne and J.C. Sens, CERN preprint.

21) R.F. Peierls, T.L. Trueman and L.L. Wang, BNL preprint 22628. See also C. Quigg, Rev. Mod. Phys. 49, 297 (1977).

22) R. Barbieri et al., Nuclear Physics B117, 50 (1976); P.V. Landshoff and D.M. Scott, Nuclear Physics B131, 172 (1977).

23) A.J. Buras and K.J.F. Gaemers, Nuclear Physics B132, 249 (1978).

24) F. Halzen and D.M. Scott, Phys. Rev. Lett., 40, 1117 (1978).

25) C. Sachrajda, Phys. Lett. 76B, 100 (1978).

26) R.D. Field, Phys. Rev. Lett. 40, 997 (1978).

27) A.P. Contogouris, XIII Rencontre de Moriond (1978).

28) C.O. Escobar, Phys. Rev. D15, 335 (1977).